

Testing and Analysis of Sensor Ports

M. Zhang, A. Frendi, and W. Thompson
The University of Alabama—Huntsville, Huntsville, Alabama

M.J. Casiano
Marshall Space Flight Center, Huntsville, Alabama

The NASA STI Program...in Profile

Since its founding, NASA has been dedicated to the advancement of aeronautics and space science. The NASA Scientific and Technical Information (STI) Program Office plays a key part in helping NASA maintain this important role.

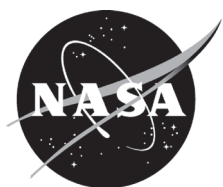
The NASA STI Program Office is operated by Langley Research Center, the lead center for NASA's scientific and technical information. The NASA STI Program Office provides access to the NASA STI Database, the largest collection of aeronautical and space science STI in the world. The Program Office is also NASA's institutional mechanism for disseminating the results of its research and development activities. These results are published by NASA in the NASA STI Report Series, which includes the following report types:

- **TECHNICAL PUBLICATION.** Reports of completed research or a major significant phase of research that present the results of NASA programs and include extensive data or theoretical analysis. Includes compilations of significant scientific and technical data and information deemed to be of continuing reference value. NASA's counterpart of peer-reviewed formal professional papers but has less stringent limitations on manuscript length and extent of graphic presentations.
- **TECHNICAL MEMORANDUM.** Scientific and technical findings that are preliminary or of specialized interest, e.g., quick release reports, working papers, and bibliographies that contain minimal annotation. Does not contain extensive analysis.
- **CONTRACTOR REPORT.** Scientific and technical findings by NASA-sponsored contractors and grantees.
- **CONFERENCE PUBLICATION.** Collected papers from scientific and technical conferences, symposia, seminars, or other meetings sponsored or cosponsored by NASA.
- **SPECIAL PUBLICATION.** Scientific, technical, or historical information from NASA programs, projects, and mission, often concerned with subjects having substantial public interest.
- **TECHNICAL TRANSLATION.** English-language translations of foreign scientific and technical material pertinent to NASA's mission.

Specialized services that complement the STI Program Office's diverse offerings include creating custom thesauri, building customized databases, organizing and publishing research results...even providing videos.

For more information about the NASA STI Program Office, see the following:

- Access the NASA STI program home page at [<http://www.sti.nasa.gov>](http://www.sti.nasa.gov)
- E-mail your question via the Internet to [<help@sti.nasa.gov>](mailto:help@sti.nasa.gov)
- Phone the NASA STI Help Desk at 757-864-9658
- Write to:
NASA STI Information Desk
Mail Stop 148
NASA Langley Research Center
Hampton, VA 23681-2199, USA



Testing and Analysis of Sensor Ports

M. Zhang, A. Frendi, and W. Thompson
The University of Alabama—Huntsville, Huntsville, Alabama

M.J. Casiano
Marshall Space Flight Center, Huntsville, Alabama

National Aeronautics and
Space Administration

Marshall Space Flight Center • Huntsville, Alabama 35812

May 2016

Acknowledgments

The experimental work was made possible by TOA Electronics, Inc. through Kevin Talmant who generously loaned The University of Alabama—Huntsville (UAH) team a Plane Wave Generator PW-1230SB which was critical to the experiments. In addition, team UAH also appreciates Tanner Smith and his colleagues at Brüel & Kjær North America Inc. for providing needed support for the Pulse Software and free licenses for the time capture module.

Available from:

NASA STI Information Desk
Mail Stop 148
NASA Langley Research Center
Hampton, VA 23681-2199, USA
757-864-9658

This report is also available in electronic form at
<<http://www.sti.nasa.gov>>

TABLE OF CONTENTS

1. BACKGROUND	1
2. EQUATIONS FOR WAVES TRAVELING IN A TUBE WITH A RIGID CAPPED END	2
2.1 Acoustic Wave Propagation in Homogeneous Medium With a Constant Temperature and Ideal Boundary Conditions	2
2.2 Wave Equation With Variable Density	6
3. ABSORPTION AND ATTENUATION OF ACOUSTIC WAVES	13
3.1 Loss to the Medium	13
3.2 Losses to the Wall	15
3.3 Loss in a Wide Pipe.....	18
4. MISCELLANEOUS	21
4.1 Justification for the Plane Wave Assumption	21
4.2 Pressure Measurement Locations	23
5. RESULTS	25
5.1 Experimental Results	25
5.2 Comparison of the Analytical Model Prediction to the Experimental Data	43
6. CONCLUSIONS	52
REFERENCES	53

LIST OF FIGURES

1.	Geometry of a sensor port	2
2.	Various components of the pressure field in the sensor port. Incident wave is blue and reflected waves are green	3
3.	Assumed temperature profile in a sensor port (a) connected to a combustion chamber and (b) connected to a cryogenic dewar	7
4.	Coordinate system for calculating losses to viscous walls: (a) Cylinder and (b) boundary layer (zoomed in very close to cylinder wall)	16
5.	Coordinate system for a cylindrical port	19
6.	Coordinate system for a cylindrical port	21
7.	Tube wall—velocity distribution in (a) axial direction and (b) radial direction	23
8.	Display of standing wave node and antinode	24
9.	Setup for the PVC pipe experiment: (a) Measured at the top of the pipe and (b) incident wave measurement	26
10.	Time history of the acoustic pressure at the end of the PVC pipe (red line), at the inlet of the pipe (green line), and at the inlet location without the pipe present (blue line)	26
11.	A pile of aluminum plates at Marshall Space Flight Center, one of which was used in the test	27
12.	Finished aluminum plate with sensor ports ready to test	27
13.	Schematic of the plate experiment: (a) Top view and (b) side view	28
14.	The as-built dimensions of the plate and sensor ports	29
15.	The as-built dimensions of the short port	29
16.	The as-built dimensions of the long port	30

LIST OF FIGURES (Continued)

17.	Suspended plate: (a) Rear view with microphones and (b) front view with the plane wave speaker	31
18.	Various components used in the experiments: (a) Temperature and humidity measurement, (b) amplifier used, (c) the pulse system input-output, and (d) the Pulse software screen display	31
19.	Microphone locations on short port configuration	32
20.	Time history of the acoustic pressure at mic1 (red), mic2 (green), and mic3 (blue) at 1,000 Hz	33
21.	SPL spectrum at various microphone locations: (a) mic1, (b) mic2, and (c) mic3	33
22.	Time history of the acoustic pressure measured at mic1 (red), mic2 (green), and mic3 (blue), and at three different frequencies: (a) 500 Hz, (b) 750 Hz, and (c) 1,500 Hz	34
23.	Response of a short port to a frequency sweep—run 7, mic1: (a) Acoustic pressure time history, (b) frequency, and (c) instantaneous pressure peak amplitude	35
24.	Time history of acoustic pressure at mic1 (red), mic2 (green), and mic3 (blue) driven from white noise	36
25.	SPL spectrum of acoustic pressure	36
26.	Transfer function between mic1 and mic3 for a random frequency plane wave	36
27.	Microphone locations on long port configuration	37
28.	Time history of acoustic pressure at mic1 (red), mic2 (green), mic3 (deep blue), mic4 (light blue), and mic5 (purple) for the long port	38
29.	SPL spectrum of the pressure at (a) mic1, mic2, and mic3; (b) mic3 and mic4; and (c) mic3 and mic5	38
30.	Transfer functions between (a) mic1 and mic3, (b) mic4 and mic3, and (c) mic5 and mic3	39

LIST OF FIGURES (Continued)

31.	Response of the long port to a frequency sweep—run 16: (a) Acoustic pressure at mic1, (b) frequency, (c) instantaneous pressure peak amplitude at mic1, (d) instantaneous pressure peak amplitude at mic4, and (e) instantaneous pressure peak amplitude at mic5	40
32.	Comparison of mic1 and mic3 at (a) 500 Hz, (b) 750 Hz, (c) 1,000 Hz, and (d) 1,500 Hz	41
33.	Comparison of mic4 and mic3 at (a) 500 Hz, (b) 750 Hz, (c) 1,000 Hz, and (d) 1,500 Hz	42
34.	Comparison of mic5 and mic3 at (a) 500 Hz, (b) 750 Hz, (c) 1,000 Hz, and (d) 1,500 Hz	43
35.	Measured and predicted SPL spectrum for plane wave input at mic1 location: (a) Random and (b) harmonic input at 1,000 Hz	44
36.	Absorption coefficient	45
37.	Transfer function gain at mic1 location	46
38.	Time history of the pressure at mic3 location for a random frequency plane wave input	47
39.	SPL spectrum at mic3 location for a random frequency plane wave input	47
40.	SPL spectrum at mic3 location using 1,500 Hz harmonic plane wave input	48
41.	SPL spectrum at mic1 location for a random frequency plane wave input: (a) sound pressure level and (b) transfer function gain	48
42.	Mic3 location for a random frequency plane wave input: (a) Time history and (b) SPL spectrum	49
43.	SPL spectrum at mic3 location for plane wave frequencies: (a) 500 Hz, (b) 750 Hz, (c) 1,000 Hz, (d) 1,250 Hz, and (e) 1,500 Hz	50
44.	Pressure distribution along the x -axis obtained using the Runge-Kutta method and the exact solution for frequencies of (a) 500 Hz and (b) 1,000 Hz	51

LIST OF FIGURES (Continued)

45.	Pressure distribution along the x -axis obtained using the Runge-Kutta method and the WKB solution for frequencies of (a) 500 Hz and (b) 1,000 Hz	51
-----	---	----

LIST OF TABLES

1.	Acoustic absorption in fluids	15
----	-------------------------------------	----

LIST OF ACRONYMS

CFD	computational fluid dynamics
OASPL	overall sound pressure level
PSD	power spectral density
SPL	sound pressure level
TF	transfer function
TP	Technical Publication
UAH	The University of Alabama—Huntsville
WKB	Wentzel-Karmers-Brillouin

NOMENCLATURE

A	arbitrary constant, function
a	radius of the port
B	arbitrary constant
b	constant
C	arbitrary constant
c	speed of sound
c_1, c_2	constants
c_p	phase speed
D	arbitrary constant
E	arbitrary constant
e	exponential
F	arbitrary constant
f	frequency, applied force
f_0	peak center frequency
f_l	frequency below the peak
f_u	frequency above the peak
g	function, constant
J	Bessel function, Jacobian
j	imaginary number
K	complex wave number

NOMENCLATURE (Continued)

\vec{k}, k_x	propagation vector
$k, \tilde{k}, \bar{k}, k_0, K$	wave number, effective wave number
L	length
L_e	effective length
l	mode number
m	mass, constant, mode number
n	index of refraction
P	complex pressure
P	pressure
P_e	effective pressure
P^I, p^I	incident wave amplitude
P_L	measured pressure
$P(L)$	measured pressure
Pr	Prandtl number
P_{ref}	reference pressure
p, p'	acoustic pressure
R	reflection coefficient, function
R_m	resistance
r	radial coordinate
s	disk area, shear wave number
T	temperature

NOMENCLATURE (Continued)

T_{∞}	ambient temperature
t	time
u'	oscillatory velocity
\vec{u}	velocity vector
u	velocity
u_0	amplitude
u_x	propagation vector
w	complex variable
X	reactance
\vec{x}	position vector
x	Cartesian coordinate
x_o	x coordinate point
y	Cartesian coordinate, variable
Z	function
z	Cartesian coordinate, complex variable
z_m	mechanical impedance
∇	gradient
\in	exists
α	absorption coefficient
α_{exp}	experimental based absorption coefficient
α_k	absorption coefficient due to thermal conductivity

NOMENCLATURE (Continued)

α_s	absorption coefficient due to viscous effects
β	temporal absorption coefficient, function
γ	specific heat ratio
δ	acoustic boundary layer thickness
η	variable
Θ	function
θ	circumferential coordinate, function
κ	thermal conductivity
λ	wavelength
μ	shear viscosity
μ_B	bulk viscosity
ν	kinematic viscosity
ξ	variable
ρ	density
ρ_0	ambient density
τ_s	relaxation time
φ	function
ϕ	function
ψ	function
ω	angular frequency

TECHNICAL PUBLICATION

TESTING AND ANALYSIS OF SENSOR PORTS

1. BACKGROUND

Dynamic pressure measurements for liquid-propellant rocket engines are used frequently for requirement verification, anomaly investigation, dynamics characterization, and model anchoring. Sensors are often mounted in nonideal configurations to protect the sensor from cryogenic fluids and hot gasses, or because of interference/fitting difficulties. Sensors that are recessed from the environment of interest lead to dynamic port resonances and port fluid freezing, while purged sensors can alter the dynamics in undesirable ways. These situations necessitate extreme care in interpreting the dynamic data because the sensor port introduces unwanted dynamics and damping characteristics. Characteristics of deadheaded cavities are also of interest, in general, since side branches, spin-start lines, stabilizing aids, or injector elements are cavities that behave similarly. Private industry, including sensor manufacturers and the hearing aid industry, would also be interested in the results.

The objective of this effort was to evaluate the dynamic response characteristics of several port configurations. These evaluations would be completed by The University of Alabama—Huntsville (UAH) using analytic models, 3D unsteady computational fluid dynamics (CFD) simulations, and experimental data from anechoic chamber testing at UAH's facility. Acoustic models and pressure transfer functions would be developed and then correlated to the testing and CFD simulations. The CFD simulations were not completed and models were only compared with experimental data.

2. EQUATIONS FOR WAVES TRAVELING IN A TUBE WITH A RIGID CAPPED END

Since the problem at hand is that of pressure measurements using sensor ports, with the pressure sensor being at one end of the port, it is therefore appropriate to consider an acoustic wave traveling in a tube with a rigid capped end.

2.1 Acoustic Wave Propagation in Homogeneous Medium With a Constant Temperature and Ideal Boundary Conditions

First, the propagation of a plane acoustic wave in a homogeneous, constant temperature medium is considered for simplicity. Figure 1 shows the dimensions of the tube with the rigid end at $x = L$.

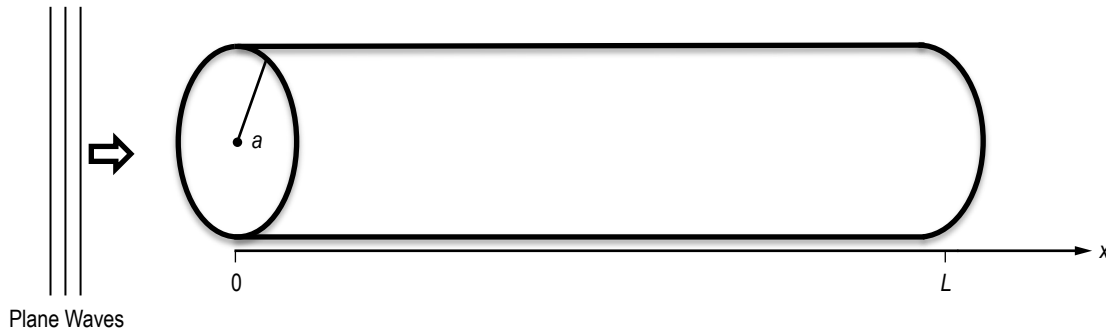


Figure 1. Geometry of a sensor port.

The governing equation for a plane acoustic wave propagating in the port in the x -direction is given by

$$\left(\frac{\partial}{\partial x^2} - \frac{1}{c^2} \frac{\partial^2}{\partial t^2} \right) p = 0, \quad (1)$$

with rigid boundary condition at $x = L$ and pressure release boundary condition at $x = 0$. A general solution of equation (1) can be written as

$$p(x, t) = A e^{j(\omega t + k(L-x))} + B e^{j(\omega t - k(L-x))} \quad (2)$$

with the first term representing the incident wave and the second term representing the reflected wave. One needs to apply the boundary conditions given above to determine A and B . The boundary at $x = 0$ is a pressure release and acoustic waves will also be reflected from this boundary. In order to capture the physics of the problem at hand, consider figure 2, which shows notionally the resultant pressure at a location, t , in the sensor port as a superposition of the incident wave, (1), with the various reflected waves (2), (3), (4), ..., etc.

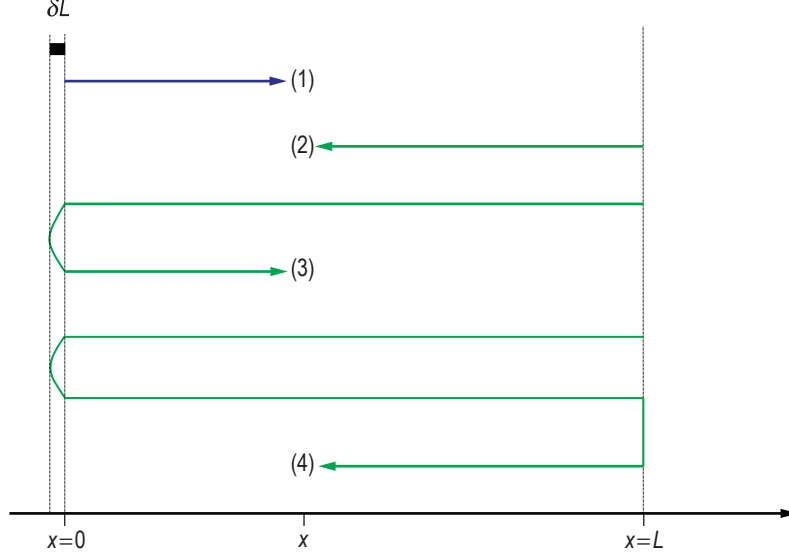


Figure 2. Various components of the pressure field in the sensor port. Incident wave is blue and reflected waves are green.

Using separation of variables, one can write the solution as

$$p(x,t) = P(x)e^{j\omega t}, \quad x \in [0, L], \quad (3)$$

where $P(x)$ contains information on wave amplitude and phase. The contribution of the incident wave (1) to the pressure at x is given by

$$P_1(x) = Ae^{jk(L-x)}, \quad (4)$$

which for $x=0$ gives $P_1(0) = P^I$ and hence $A = P^I e^{-jkL}$, where P^I is the incident wave amplitude. In figure 2 and for waves (3), (4), and higher, $L_e = L + \delta L$ is the effective length traveled by the reflected wave with $\delta L = 0.85a$ for a flanged sensor port and $\delta L = 0.6a$ for an unflanged sensor port and a the radius of the port.¹⁻³ In our primary experiment, the sensor port is considered flanged because a large plate extends away from the port at the opening.

The reflected wave (2) contributes to the pressure field at x as

$$P_2(x) = Be^{-jk(L-x)}. \quad (5)$$

Reflected wave (3) has a contribution to the pressure field at x as follows:

$$P_3(x) = Ce^{-jk[2L_e - (L-x)]} = Ce^{-2jkL_e} e^{jk(L-x)} \text{ with } x \in [-\delta L, L]. \quad (6)$$

Reflected wave (4) has a contribution to the pressure field at x as follows:

$$P_4(x) = De^{-jk[2L_e + (L-x)]} = De^{-2jkL_e} e^{-jk(L-x)}. \quad (7)$$

Using what is known about the boundary conditions, the rigid boundary at $x=L$ means

$$A = B, C = D, \dots \quad (8)$$

because the reflection coefficient $R=1$.

The pressure release boundary condition at $x=0$ results in

$$R = \frac{C}{B} = \frac{\left[1 - 0.5(ka)^2\right] - j0.85(ka)}{\left[1 + 0.5(ka)^2\right] + j0.85(ka)} = c_1, \quad (9)$$

and $c_1 \approx -1$ at low frequencies.

The analysis above is carried out without taking into account any losses in the medium. When losses are included, the above equations can be rewritten as follows:

$$\text{Wave (1): } P_1(x) = Ae^{jk(L-x)}e^{-\alpha x}, \quad (10)$$

$$\text{Wave (2): } P_2(x) = Be^{-jk(L-x)}e^{-\alpha L}e^{-\alpha(L-x)}, \quad (11)$$

$$\text{Wave (3): } P_3(x) = Ce^{-jk2L_e}e^{jk(L-x)}e^{-2\alpha L}e^{-\alpha x}, \quad (12)$$

and

$$\text{Wave (4): } P_4(x) = De^{-jk2L_e}e^{-jk(L-x)}e^{-3\alpha L}e^{-\alpha(L-x)}. \quad (13)$$

In the above equations, α is the absorption coefficient in the medium and will be defined in section 3. The total pressure field at a location x in the port results from the superposition of the different waves as follows:

$$P(x) = \sum_{i=1}^{\infty} P_i(x) = P_1(x) + P_2(x) + P_3(x) + P_4(x) + \dots \quad (14)$$

and after using equations (10)–(13) becomes

$$P(x) = A \left[\left(e^{jk(L-x)}e^{-\alpha x} + e^{-jk(L-x)}e^{-\alpha L}e^{-\alpha(L-x)} \right) + (c_1) \left(e^{-jk2L_e}e^{jk(L-x)}e^{-2\alpha L}e^{-\alpha x} \right. \right. \\ \left. \left. + e^{-jk2L_e}e^{-jk(L-x)}e^{-3\alpha L}e^{-\alpha(L-x)} \right) + \dots \right]. \quad (15)$$

Including $P_5(x)$ and $P_6(x)$ such that

$$\text{Wave (5): } P_5(x) = E e^{-jk4L_e} e^{jk(L-x)} e^{-4\alpha L} e^{-\alpha x} \quad (16)$$

and

$$\text{Wave (6): } P_6(x) = F e^{-jk4L_e} e^{-jk(L-x)} e^{-5\alpha L} e^{-\alpha(L-x)} \quad (17)$$

will help allow one to observe a pattern in each of the terms.

With $E = F$, $\frac{E}{D} = c_1$ and referring to equations (8) and (9), it can be shown that $E = F = (c_1)^2 A$. With this coefficient simplification and the addition of waves (5) and (6) to equation (15), one obtains

$$\begin{aligned} P(x) = & A e^{jk(L-x)} e^{-\alpha x} \left[1 + (c_1) e^{-j2kL_e} e^{-2\alpha L} + (c_1)^2 \left(e^{-j2kL_e} e^{-2\alpha L} \right)^2 + \dots \right] \\ & + A e^{-jk(L-x)} e^{-\alpha L} e^{-\alpha(L-x)} \left[1 + (c_1) e^{-j2kL_e} e^{-2\alpha L} + (c_1)^2 \left(e^{-j2kL_e} e^{-2\alpha L} \right)^2 + \dots \right] \end{aligned} \quad (18)$$

which can be written as

$$\begin{aligned} P(x) = & \left[1 + (c_1) e^{-j2kL_e} e^{-2\alpha L} + (c_1)^2 \left(e^{-j2kL_e} e^{-2\alpha L} \right)^2 + \dots \right] \\ & \times \left[A e^{jk(L-x)} e^{-\alpha x} + A e^{-jk(L-x)} e^{-\alpha L} e^{-\alpha(L-x)} \right]. \end{aligned} \quad (19)$$

It is recognized that the first term is of the form $\left[1 + y + y^2 + \dots \right]$ with $y = (c_1) e^{-j2kL_e} e^{-2\alpha L}$. This geometric sum, $\frac{1}{1-y}$, converges for $|y| < 1$, which makes equation (19) become

$$P(x) = A \frac{e^{jk(L-x)} e^{-\alpha x} + e^{-jk(L-x)} e^{-\alpha(2L-x)}}{1 - c_1 e^{-j2kL_e} e^{-2\alpha L}}. \quad (20)$$

Using the fact that $A = P^I e^{-jkL}$, equation (20) becomes

$$\frac{P(x)}{P^I} = \frac{e^{-jkx} e^{-\alpha x} + e^{-jk(2L-x)} e^{-\alpha(2L-x)}}{1 - c_1 e^{-j2kL_e} e^{-2\alpha L}} = g(x). \quad (21)$$

This equation represents the pressure amplitude at any location x relative to the pressure amplitude of the incident wave. And, in particular, at $x = L$, one gets

$$\frac{P(L)}{P^I} = \frac{2e^{-jkL}e^{-\alpha L}}{1 - c_1 e^{-j2kL}e^{-2\alpha L}}, \quad (22)$$

which one can use in either direction, depending on available experimental data. In other words, in the forward direction, the incident pressure amplitude, P^I , can be used to predict the pressure amplitude in the back of the port, $P(L)$. And in the reverse direction, the pressure amplitude in the back of the port can be used to predict the incident pressure amplitude. One can write equation (21) as

$$P(x) = P^I g(x), \quad (23)$$

and reconstructing $p(x, t)$ for a harmonic field, one gets

$$p(x, t) = P(x)e^{j\omega t} = P^I g(x)e^{j\omega t}. \quad (24)$$

For multiple frequencies, one can write

$$p(x, t)|_{\omega} = P(x, \omega)e^{j\omega t} = P^I(\omega)g(x, \omega)e^{j\omega t} \text{ with } \omega \in [-\infty, +\infty] \quad (25)$$

with

$$P^I(\omega) = \frac{1}{2\pi} \int P^I(t)e^{-j\omega t} dt; \quad (26)$$

therefore,

$$p(x, t) = \int P(x, \omega)e^{j\omega t} d\omega = \int P^I(\omega)g(x, \omega)e^{j\omega t} d\omega. \quad (27)$$

2.2 Wave Equation With Variable Density

In this section, the constant temperature assumption made previously will be removed. The wave equation with variable density allows for implementation of a variable equilibrium temperature profile (not a fluctuating temperature, but a varying mean temperature). References 4–6 provide more details on the derivation of a variable mean density wave equation. Assuming no flow, the wave equation with variable density is given as

$$\nabla^2 p - \frac{\nabla \rho_0}{\rho_0} \nabla p - \frac{1}{c^2} \frac{\partial^2 p}{\partial t^2} = 0, \quad (28)$$

where $p = p(\vec{x}, t)$ is the acoustic pressure, $\rho_0 = \rho_0(\vec{x})$ is the equilibrium density, and $c = c(\vec{x})$ is the sound speed. Note that the equilibrium density is a function of space. The one-dimensional form is given as

$$\frac{\partial^2 p}{\partial x^2} - \frac{1}{\rho_0} \frac{\partial \rho_0}{\partial x} \frac{\partial p}{\partial x} - \frac{1}{c^2} \frac{\partial^2 p}{\partial t^2} = 0. \quad (29)$$

These equations can easily be solved numerically,⁵ however, insight can be gleaned by examining some of the analytic solutions.

2.2.1 Acoustic Wave Propagation in a Medium With a Temperature Gradient Using the Wentzel-Karmers-Brillouin Method⁶

An experiment may be that of a combustion chamber at high temperature or a cryogenic dewar at low temperature with a sensor port for measurement. For a combustion chamber at high temperature, for example, the inlet of the sensor port opening will be a higher temperature followed by a decaying temperature in the sensor port. Figure 3 (a) and (b) illustrate the extent of the duct for a high-temperature combustion chamber and a cryogenic dewar, respectively. The port length extends from $x=0$ to $x=L$. The temperature profile for the port may follow a form such as $T(x) = be^{-gx} + T_\infty$ with $g > 0$ where T_∞ is the temperature at the back of the sensor port and $T(x)$ is the absolute temperature at the spatial location x .

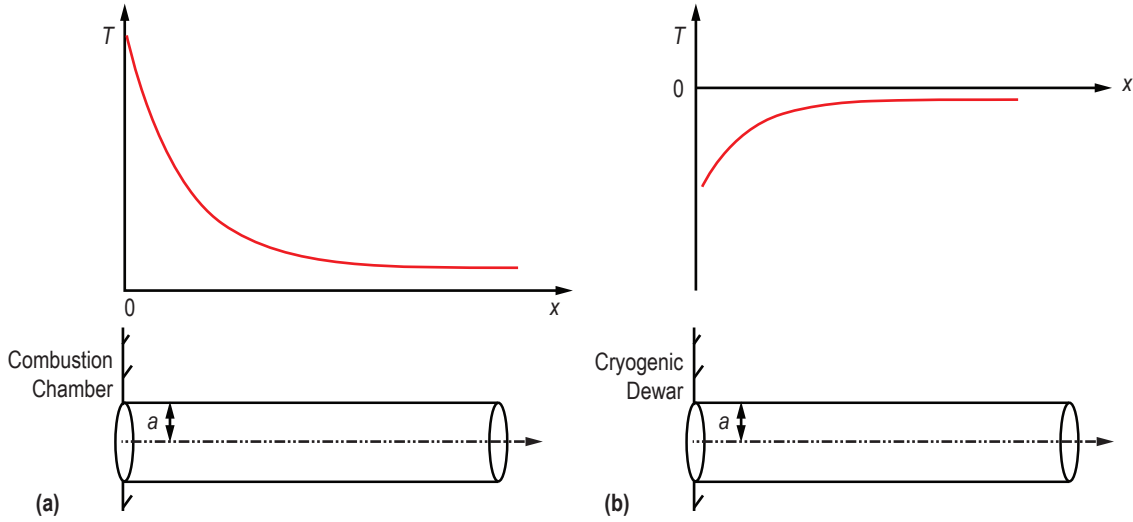


Figure 3. Assumed temperature profile in a sensor port (a) connected to a combustion chamber and (b) connected to a cryogenic dewar.

A solution to equation (29) is assumed to be in the form $p(x,t) = P(x)e^{-j\omega t}$ and equation (29) becomes

$$\frac{d^2 P}{dx^2} - \frac{1}{\rho_0} \frac{d\rho_0}{dx} \frac{dP}{dx} + \tilde{k}^2 P = 0, \quad (30)$$

where $\tilde{k}^2 = \tilde{k}(x)^2 = \omega^2 / c(x)^2$ is the wave number.

The Wentzel-Karmers-Brillouin (WKB) method has been used to solve the variable coefficient Helmholtz equation, $d^2 P / dx^2 + \tilde{k}(x)^2 P = 0$. Further details of the WKB method are discussed in reference 6. To use the WKB method, equation (30) needs to be transformed into a standard form of a variable coefficient Helmholtz equation.

A new variable is defined as

$$y(x) = \frac{P(x)}{\sqrt{\rho_0(x)}}. \quad (31)$$

To simplify notation, the spatial variable is ignored. The prime symbol in the following will be used to represent derivatives with respect to the spatial variable. Equation (31) can be written with first and second derivatives as

$$\begin{aligned} P &= y\sqrt{\rho_0} \\ \frac{dP}{dx} &= \frac{1}{2} \frac{\rho_0'}{\sqrt{\rho_0}} y + y' \sqrt{\rho_0} \\ \frac{d^2 P}{dx^2} &= y'' \sqrt{\rho_0} + \frac{y' \rho_0'}{\sqrt{\rho_0}} + \left(\frac{1}{2} \frac{\rho_0''}{\sqrt{\rho_0}} - \frac{1}{4} \frac{\rho_0'^2}{\rho_0 \sqrt{\rho_0}} \right) y. \end{aligned} \quad (32)$$

Substituting equation (32) into equation (30) gives

$$y'' + \bar{k}^2 y = 0, \quad (33)$$

where $\bar{k}^2 = \tilde{k}^2 + \frac{1}{2} \frac{\rho_0''}{\rho_0} - \frac{3}{4} \left(\frac{\rho_0'}{\rho_0} \right)^2$. Using the state equation, $p_0/\rho_0 = RT$ to linearize $\rho_0 = \rho_0(T)$ gives

$$\rho_0' / \rho_0 = -T' / T, \text{ and with some manipulation, } \bar{k}^2 = \tilde{k}^2 - \frac{1}{2} \frac{T''}{T} + \frac{1}{4} \left(\frac{T'}{T} \right)^2.$$

To simplify notation further, the wave number is defined as

$$k^2 = |\bar{k}^2| = \left| \tilde{k}^2 - \frac{1}{2} \frac{T''}{T} + \frac{1}{4} \left(\frac{T'}{T} \right)^2 \right|. \quad (34)$$

Three possible cases are written below. Cases 1 and 2 are simpler to examine and are described separately:

- Case 1: $y'' + k^2 y = 0$, $\bar{k}^2 > 0$ for $x \in (0, L)$
- Case 2: $y'' - k^2 y = 0$, $\bar{k}^2 < 0$ for $x \in (0, L)$
- Case 3: $y'' - k^2 y = 0$, $\bar{k}^2 < 0$ for $x \in (0, x_0)$
 $y'' + k^2 y = 0$, $\bar{k}^2 > 0$ for $x \in (x_0, L)$ with $k(x_0)^2 = 0$.

For case 1, the wave equation with variable wave number as a function of space can be solved using the WKB method. It is noted that a linear profile of $T(x) = a + bx$ will satisfy this case for all frequency ranges. Reference 6 shows that the lossy WKB solution is given by

$$P(x) \sqrt{\frac{k}{\rho_0}} = P^I \sqrt{\frac{k(0)}{\rho_0(0)}} e^{-j\theta(L)} \left(e^{j[\theta(L) - \theta(x)]} + e^{-j[\theta(L) - \theta(x)]} \right), \quad (35)$$

where $\theta(x) = \int_0^x \hat{k}(\beta) d\beta = \int_0^x (k(\beta) - j\alpha(\beta)) d\beta$. And using a similar procedure as in section 2.1, the solution becomes

$$\frac{P(x)}{P^I} \sqrt{\frac{k\rho_0(0)}{\rho_0 k(0)}} = \frac{e^{-j\theta(x)} e^{-\alpha x} + e^{-j[2\theta(L) - \theta(x)]} e^{-\alpha[2L - x]}}{1 - c_1 e^{-j2\theta(L_e)} e^{-2\alpha L}}, \quad (36)$$

where $\alpha x = \int_0^x \alpha(\beta) d\beta$, $\theta(x) = \int_0^x k(\beta) d\beta$, $\theta(L_e) = k(0)\delta L + \int_0^x k(\beta) d\beta$, and c_1 is the reflection coefficient further described in section 2.1.

For case 2, the solution method follows a similar approach to the WKB method. The solution is assumed to follow the form of $y = \theta(x)$ and the lossy solution becomes

$$\frac{P(x)}{P^I} \sqrt{\frac{\rho_0(0)}{\rho_0}} = \frac{e^{-j\theta(x)} e^{-\alpha x} + m e^{-[2\theta(L) - \theta(x)]} e^{-\alpha[2L - x]}}{1 - c_1 m e^{-2\theta(L_e)} e^{-2\alpha L}}, \quad (37)$$

where $m = \frac{\theta'(L) - \rho'_0(L) / [2\rho_0(L)]}{\theta'(L) + \rho'_0(L) / [2\rho_0(L)]}$.

2.2.2 Acoustic Wave Propagation in a Medium With a Temperature Gradient Using Conformal Mapping^{7,8}

This method is not recommended for application because it applies specifically to 2D problems; however, it does provide some insight into the solution form.

This section considers the wave equation in a nonhomogeneous medium. A derivation of the nonhomogeneous medium has been described previously using Euler equations and continuity such as in reference 8. Simplifying the notation from equation (28), equation (38) is written as

$$\nabla^2 p + k^2 p - \frac{\nabla \rho}{\rho} \nabla p = 0. \quad (38)$$

The density and sound speed (or wave number) vary as a function of space while pressure is a function of space and time. In general, this equation can be solved numerically. The functional forms of the variables p , k , and ρ are $p(x,y,t)$, $k(x,y)$, and $\rho(x,y)$. A conformal mapping approach will be used and so the space variables must be two dimensional.

In a similar fashion, a wave equation for varying temperature and sound speed (or wave number) can be derived by linearizing the state equation as $\rho = \rho(T)$:

$$\nabla^2 p + k^2 p + \frac{\nabla T}{T} \nabla p = 0. \quad (39)$$

Equation (38) will be examined here. A new variable is first introduced to simplify the procedure shown in equation (40). The functional form of the variable ϕ is $\phi(x,y,t)$:

$$\phi = \frac{p}{\sqrt{\rho}}. \quad (40)$$

Equation (38) can be reduced by substituting in equation (40). Similar to equations (31)–(33), the reduced gradient form of the equations, equations (41) and (42) follow where the functional form of the variable K is $K(x,y)$:

$$\nabla^2 \phi + K^2 \phi = 0 \quad (41)$$

and

$$K^2 = k^2 + \frac{\nabla^2 \rho}{2\rho} - \frac{3}{4} \left(\frac{\nabla \rho}{\rho} \right)^2. \quad (42)$$

If the space dimensions are taken as 2D Cartesian, a complex change of variables known as conformal mapping can be used to develop a tractable form of the Helmholtz equation. The conformal mapping approach is restrictive in this sense, however, a 2D solution provides insight and solutions that can be studied or used in some simple practical cases. This was the goal of reference 7 and equation (38) was successfully transformed into a constant coefficient Helmholtz equation.

If the density variation is small over the wavelength, then the second and third terms of equation (42) can be neglected. The 2D Helmholtz equation with variable coefficient results in equation (43):

$$\frac{\partial^2 \varphi}{\partial x^2} + \frac{\partial^2 \varphi}{\partial y^2} + k^2 \varphi = 0. \quad (43)$$

Using Snell's law, $k_0 \sin \theta_0 = k \sin \theta$ and the index of refraction is given by $n = k/k_0 = c_0/c$. Substituting this relationship into equation (43) gives equation (44). The purpose of this step is so a later coordinate transformation can be used to convert the equation into a constant coefficient Laplace equation. The functional form of the variable n is $n(x, y)$:

$$\frac{\partial^2 \varphi}{\partial x^2} + \frac{\partial^2 \varphi}{\partial y^2} + k_0^2 n^2 \varphi = 0. \quad (44)$$

But first, the equation is mapped into the complex domain. The complex variable can be written as $z = x + jy$ with complex conjugate $\bar{z} = x - jy$. The Wirtinger derivatives, shown in equations (45) and (46), can be used to transform equation (44):

$$\frac{\partial}{\partial z} = \frac{1}{2} \left(\frac{\partial}{\partial x} - j \frac{\partial}{\partial y} \right) \quad (45)$$

and

$$\frac{\partial}{\partial \bar{z}} = \frac{1}{2} \left(\frac{\partial}{\partial x} + j \frac{\partial}{\partial y} \right). \quad (46)$$

The 2D Helmholtz with variable coefficient shown in equation (43) then becomes equation (47). The functional form of the variables φ and n are $\varphi(z, \bar{z}, t)$ and $n(z, \bar{z})$:

$$\frac{\partial^2 \varphi}{\partial z \partial \bar{z}} + \frac{1}{4} k_0^2 n^2 \varphi = 0. \quad (47)$$

Now, a coordinate transformation is used to convert this to a 2D Helmholtz equation with constant coefficient. The transformation is made where $w = f(z)$ which transforms the plane z into a plane w . The complex variables can be written as $w = \xi + j\eta$ with complex conjugate $\bar{w} = \xi - j\eta$. The relationship between the two coordinate systems is given by $\xi = \xi(x, y)$ and $\eta = \eta(x, y)$. Equation (47) can then be transformed into equation (48). The functional form of the variables φ and n are $\varphi(w, \bar{w}, t)$ and $n(w, \bar{w})$:

$$\left| \frac{\partial w}{\partial z} \right|^2 \cdot \frac{\partial^2 \varphi}{\partial w \partial \bar{w}} + \frac{1}{4} k_0^2 n^2 \varphi = 0. \quad (48)$$

It has been shown in reference 9 that the index of refraction follows the following form with a transformation of the coordinate plane and the Jacobian determinant:

$$n^2(w, \bar{w}) = n^2(\xi, \eta) = \left| \frac{\partial w}{\partial z} \right|^2. \quad (49)$$

The final form can then be written as a 2D Helmholtz equation with constant coefficient by substituting equation (49) into equation (48). The functional form of the variable φ is $\varphi(w, \bar{w}, t)$:

$$\frac{\partial^2 \varphi}{\partial w \partial \bar{w}} + \frac{1}{4} k_0^2 \varphi = 0. \quad (50)$$

Solving equation (50) in the complex plane requires obtaining a mapping that satisfies the desired behavior. For example, if n^2 varies as e^{2x} , then $f(z)$ is given by $w = e^z$ since the Jacobian in equation (51) of this mapping results in e^{2x} :

$$J = \left| \frac{\partial w}{\partial z} \right|^2 = \left(\frac{\partial \xi}{\partial x} \right)^2 + \left(\frac{\partial \eta}{\partial y} \right)^2 = \frac{\partial \xi}{\partial x} \frac{\partial \eta}{\partial x} - \frac{\partial \xi}{\partial y} \frac{\partial \eta}{\partial y}. \quad (51)$$

A solution of equation (50) is further described in reference 7. But for example, the transmitted wave solution is generally written as

$$\varphi^t = C e^{jk(\xi \sin \theta' + \eta \cos \theta')} \quad (52)$$

with

$$\theta' = \sin^{-1} \left(\frac{\sin \theta}{n} \right). \quad (53)$$

For a specific example, the mapping can be written as equation (54) where $f(z)$ is given by $w = e^z$:

$$\xi + j\eta = e^{x+jy} = e^x (\cos y + j \sin y). \quad (54)$$

The transmitted wave solution from equation (52) can then be written as equation (55):

$$\varphi^t = C e^{jk(e^x \cos(y) \sin \theta' + e^x \sin(y) \cos \theta')}. \quad (55)$$

Lastly, it is noted that using equation (49), equation (44) can also be written as

$$\frac{\partial^2 \varphi}{\partial x^2} + \frac{\partial^2 \varphi}{\partial y^2} + k_0^2 \left| \frac{\partial w}{\partial z} \right|^2 \varphi = 0. \quad (56)$$

While this is not necessarily a constant coefficient form of the 2D Helmholtz equation, analytic solutions may still exist.

3. ABSORPTION AND ATTENUATION OF ACOUSTIC WAVES

In the following, it is assumed that the effects of independent sources of acoustic losses can be superimposed such that the total absorption coefficient is the sum of absorption coefficients of individual loss mechanisms calculated as if each were operating alone. Reference 1, chapter 8 provides additional details.

3.1 Loss to the Medium

3.1.1 Absorption From Viscosity

Starting with the Navier-Stokes equation,

$$\rho \left[\frac{\partial \vec{u}}{\partial t} + (\vec{u} \cdot \nabla) \vec{u} \right] = -\nabla p + \left(\frac{4}{3} \mu + \mu_B \right) \nabla (\nabla \cdot \vec{u}) - \mu \nabla \times \nabla \times \vec{u} , \quad (57)$$

where μ represents the shear viscosity and μ_B the bulk viscosity, the linear continuity equation is given by

$$\nabla \cdot \vec{u} = -\frac{\partial s}{\partial t} , \quad (58)$$

where s is the acoustic density. For an adiabatic process, $p = \rho_0 c^2 s$.

Neglecting losses to the wall, one can write equation (57) as

$$\rho \left[\frac{\partial \vec{u}}{\partial t} + (\vec{u} \cdot \nabla) \vec{u} \right] = -\nabla p + \left(\frac{4}{3} \mu + \mu_B \right) \nabla (\nabla \cdot \vec{u}) . \quad (59)$$

Combining equations (57) and (58), one can obtain the lossy wave equation given by

$$\left(1 + \tau_s \frac{\partial}{\partial t} \right) \nabla^2 p = \frac{1}{c^2} \frac{\partial^2 p}{\partial t^2} , \quad (60)$$

with $\tau_s = \frac{\left(\frac{4}{3} \mu + \mu_B \right)}{\rho_0 c^2}$ and represents the relaxation time associated with viscosity.

Assuming $p = \mathbf{P}e^{j\omega t}$, equation (60) leads to the lossy Helmholtz equation:

$$\left(\frac{\partial^2}{\partial x^2} + \mathbf{K}^2 \right) \mathbf{P} = 0, \quad (61)$$

with $\mathbf{K} = k - j\alpha_s = \frac{\left(\frac{\omega}{c} \right)}{(1 + j\omega\tau_s)^{1/2}}$. Solving for the spatial absorption coefficient, α_s , and the phase speed, c_p gives

$$\alpha_s = \frac{\omega}{c} \frac{1}{\sqrt{2}} \left[\frac{\sqrt{1 + (\omega\tau_s)^2} - 1}{1 + (\omega\tau_s)^2} \right]^{1/2}, \quad c_p = \frac{\omega}{k} = c\sqrt{2} \left[\frac{1 + (\omega\tau_s)^2}{\sqrt{1 + (\omega\tau_s)^2} + 1} \right]^{1/2}. \quad (62)$$

Therefore, for a plane wave traveling in the x -direction, one can write the solution as

$$\mathbf{P} = P_0 e^{j(\omega t - \mathbf{K}x)} = P_0 e^{-\alpha_s x} e^{j(\omega t - kx)}. \quad (63)$$

Since the theory is appropriate only for $\omega \cdot \tau_s \ll 1$, then

$$\alpha_s \approx \frac{1}{2} \frac{\omega}{c} \omega \tau_s = \frac{\omega^2}{2\rho_0 c^3} \left(\frac{4}{3} \mu + \mu_B \right) \text{ and } c_p = c \left[1 + \frac{3}{8} (\omega\tau_s)^2 \right]. \quad (64)$$

3.1.2 Absorption Due to Thermal Conduction

One can show that the absorption coefficient due to thermal conduction using the heat diffusion equation is given by:¹

$$\alpha_\kappa = \frac{\omega^2}{2\rho_0 c^3} \frac{(\gamma - 1)\kappa}{c_p}, \quad (65)$$

where c_p is the specific heat at constant pressure and κ is the thermal conductivity.

3.1.3 Classical Absorption Coefficient

The combined absorption coefficient due to viscous and heat conduction losses to the medium is given by

$$\alpha = \alpha_s + \alpha_\kappa = \frac{\omega^2 \mu}{2\rho_0 c^3} \left(\frac{4}{3} + \frac{\gamma-1}{\text{Pr}} \right) = \frac{\omega^2 \nu}{2c^3} \left(\frac{4}{3} + \frac{\gamma-1}{\text{Pr}} \right). \quad (66)$$

Table 1 shows comparative data of calculated and observed values of the absorption coefficient for representative gases and liquids. The last column is the absorption calculated based on a frequency of 1,000 Hz and a tube length of 1 m. These values show that losses to the medium, for the application here, are negligible, however, it will be seen that losses to the wall will be important.

Table 1. Acoustic absorption in fluids.¹

Data for $T=20\text{ }^\circ\text{C}$ $p=1\text{ atm}$	$\alpha/f^2\text{ (Np}\cdot\text{s}^2/\text{m)}$				
	Shear Viscosity	Thermal Conductivity	Classical	Observed	$e^{-\alpha L}$
Gases	Multiply by 10^{-11}				
Argon	1.08	0.77	1.85	1.87	0.9999815
Helium	0.31	0.22	0.53	0.54	0.9999947
Oxygen	1.14	0.47	1.61	1.92	0.9999839
Nitrogen	0.96	0.39	1.35	1.64	0.9999865
Air (dry)	0.99	0.38	1.37	α/f peaks at 40 Hz	1
Carbon dioxide	1.09	0.31	1.40	α/f peaks at 30 kHz	0.9874790
Liquids	Multiply by 10^{-15}				
Glycerin	3,000		3,000	3,000	0.9999997
Mercury		6	6.0	5	1
Acetone	6.5	0.5	7.0	30	1
Water	8.1		8.1	25	1
Seawater	8.1		8.1	*	1

* α/f peaks at 1.2 and 136 kHz.

3.2 Losses to the Wall

Starting from equation (57) and neglecting $\left(\frac{4}{3}\mu + \mu_B\right)\nabla(\nabla \cdot \vec{u})$ since the absorption arising from shear at the boundary is examined here, one can write

$$\rho_0 \left[\frac{\partial \vec{u}}{\partial t} + (\vec{u} \cdot \nabla) \vec{u} \right] = -\nabla p - \mu \nabla \times \nabla \times \vec{u}. \quad (67)$$

Assuming that a plane wave in the z -direction with a propagation vector k_x parallel to the x -axis (fig. 4), the particle velocity associated with the primary wave is given by

$$u_x(x,t) = u_0 e^{j(\omega t - k_x x)}, \quad (68)$$

where $k_x = k \hat{e}_x$ and u_0 is the amplitude. Associated with the primary wave is an acoustic pressure, p , that is also a function only of (x,t) where both u_x and p satisfy Euler's equation (eq. 67) with $\mu=0$. The secondary wave, due to the presence of the wall, generates a velocity, u' , which varies with x , z , and t , leading to a total particle velocity of

$$\vec{u} = (u_x + u') \hat{e}_x. \quad (69)$$

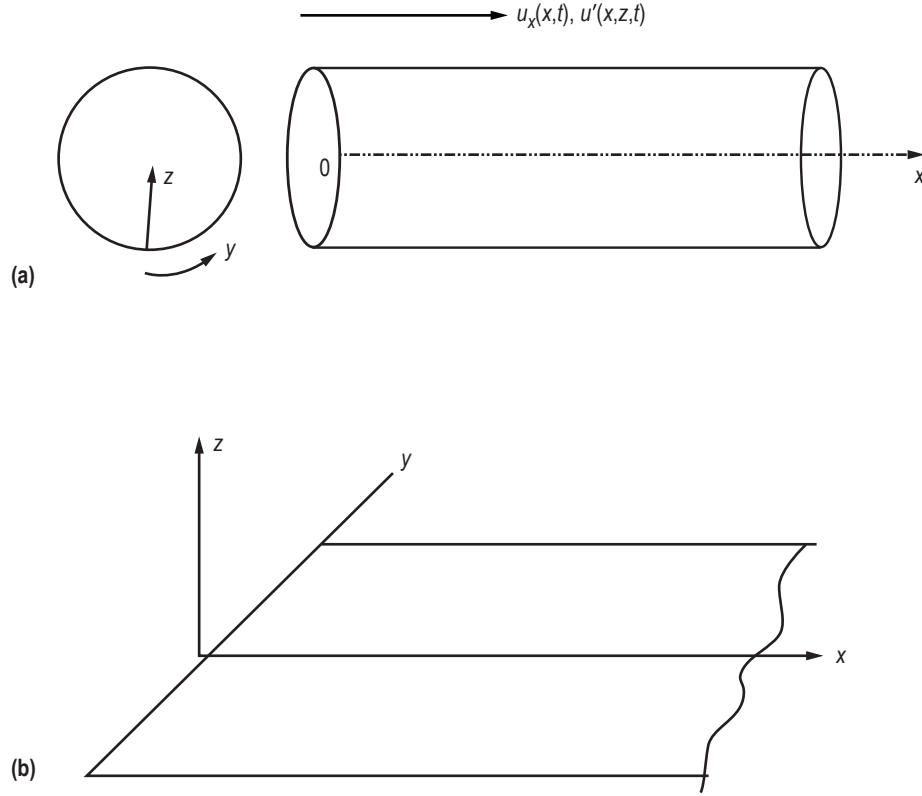


Figure 4. Coordinate system for calculating losses to viscous walls:
(a) Cylinder and (b) boundary layer (zoomed in very close to cylinder wall).

The boundary conditions are ‘no slip’:

$$\vec{u}_{z=0} = 0 \rightarrow u'_{z=0} = -u_x \quad (70)$$

and u' vanishing at large z :

$$u'_{z \rightarrow \infty} = 0. \quad (71)$$

Associated with u' is a pressure p' , and both satisfy

$$\rho_0 \frac{\partial u'}{\partial t} + \frac{\partial p'}{\partial x} = \mu \frac{\partial^2 u'}{\partial z^2}, \quad (72)$$

$$\frac{\partial p'}{\partial y} = 0, \quad (73)$$

and

$$\frac{\partial p'}{\partial z} = \mu \frac{\partial^2 u'}{\partial z \partial x}. \quad (74)$$

As will be shown later, $\frac{\partial p'}{\partial x} \approx 0$, then

$$\frac{\partial u'}{\partial t} = \frac{\mu}{\rho_0} \frac{\partial^2 u'}{\partial z^2}. \quad (75)$$

Now let $u' = A(z)e^{j\omega t}$, using equation (72) leads to

$$j\omega A(z)e^{j\omega t} = \frac{\mu}{\rho_0} e^{j\omega t} A''(z), \text{ and hence } A''(z) - j \frac{\omega \rho_0}{\mu} A(z) = 0, \quad (76)$$

therefore,

$$A(z) = c_1 e^{(1+j)z/\delta} + c_2 e^{-(1+j)z/\delta}, \text{ with } \delta = \left(\frac{2\mu}{\omega \rho_0} \right)^{1/2} = \left(\frac{2\nu}{\omega} \right)^{1/2}. \quad (77)$$

In the above equation, δ represents the acoustic boundary layer thickness, or skin depth.

The boundary conditions satisfied by A are

$$\begin{aligned} A(z)_{z \rightarrow \infty} &= \text{finite} \rightarrow c_1 = 0, \text{ and hence, } A(z) = c_2 e^{-(1+j)z/\delta} \\ A(z)_{z=0} &= -u_x, \text{ and hence, } u' = -u_x e^{-(1+j)z/\delta}. \end{aligned} \quad (78)$$

Therefore, the total velocity is

$$\vec{u} = u_x \left(1 - e^{-\frac{(1+j)z}{\delta}} \right). \quad (79)$$

The following shows that $\frac{\partial p'}{\partial x} \approx 0$. When $k\delta \ll 1$, i.e., $\frac{\delta}{\lambda} \ll 1$, equation (74) can be simplified:

$$\frac{\partial p'}{\partial z} = \mu \frac{\partial^2 u'}{\partial z \partial x} \rightarrow p' = \mu \frac{\partial u'}{\partial x}, \quad (80)$$

which leads to $\frac{\partial p'}{\partial x} = \mu \frac{\partial^2 u'}{\partial x^2}$. Substituting u' from equation (78) with equation (68) gives $\frac{\partial p'}{\partial x} = (jk)^2 \mu u'$. In a similar fashion, $\rho_0 \frac{\partial u'}{\partial t} = \rho_0 j \omega u'$. Comparing the magnitudes of the first two terms on the left-hand side of equation (72),

$$\left| \frac{\partial p'}{\partial x} \right| / \left| \rho_0 \frac{\partial u'}{\partial t} \right| = \frac{k^2 \mu}{\rho_0 \omega} = \frac{1}{2} \frac{2\mu}{\rho_0 \omega} k^2 = \frac{1}{2} (k\delta)^2, \quad (81)$$

and when $k\delta \ll 1$, i.e., $\frac{\delta}{\lambda} \ll 1$, $\left| \frac{\partial p'}{\partial x} \right|$ can be neglected compared to $\left| \rho_0 \frac{\partial u'}{\partial t} \right|$.

3.3 Loss in a Wide Pipe

A harmonic plane wave is assumed to propagate in a pipe of radius a , with air as the medium, in standard conditions; $T = 300$ K, $p = 1$ atm. The frequency range of interest in the experiment is $f \in (10 \text{ Hz}, 5,000 \text{ Hz})$. If a case similar to the experiment in this Technical Publication (TP) with pipe

radius $a = 0.25$ inch, $a \gg \delta$, i.e., the radius of the pipe is much larger than the skin depth, so the results from section 3.2 can be applied (in this case, $f = 10$ Hz, $a/\delta \approx 10$; $f = 100$ Hz, $a/\delta \approx 32$; and $f = 1,000$ Hz, $a/\delta \approx 98$).

Consider a disk of the fluid in a port with thickness dx and mass m , as shown in figure 5:

$$s = \pi a^2, f = m \frac{\partial u}{\partial t}, \quad (82)$$

with s the disk area and f the applied force. The mechanical impedance associated with the disk presented to the force is

$$z_m = f / \langle u \rangle_s. \quad (83)$$

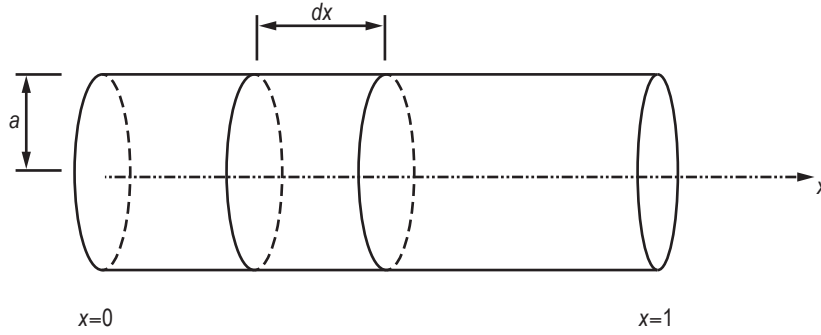


Figure 5. Coordinate system for a cylindrical port.

Using $u = u_x \left(1 - e^{-(1+j)z/\delta}\right)$ and a coordinate transformation, the area averaged velocity is

$$\langle u \rangle_s = \frac{u_x}{\pi a^2} \int_s \left(1 - e^{-(1+j)z/\delta}\right) ds = u_x \left[1 - \frac{2\pi}{\pi a^2} \int_0^a e^{-\frac{1+j}{\delta}(a-r)} r dr \right]. \quad (84)$$

The following integral can be evaluated as

$$\int_0^a e^{-\frac{(1+j)}{\delta}(a-r)} r dr = \left\{ \left[\frac{\delta}{1+j} \cdot r - \left(\frac{\delta}{1+j} \right)^2 \right] \cdot e^{-\frac{(1+j)}{\delta}(a-r)} \right\}_0^a \quad (85)$$

and with $\frac{a}{\delta} \gg 1 \rightarrow e^{-(1+j)a/\delta} \approx 0$, this integral simplifies to $\int_0^a e^{-\frac{(1+j)}{\delta}(a-r)} \cdot r dr = \frac{\delta}{1+j} a - \left(\frac{\delta}{1+j} \right)^2$.

Substituting this reduced integral into equation (84) gives

$$\begin{aligned}
\langle u \rangle_s &= u_x \left[1 - \frac{2}{a^2} \left(\frac{\delta}{1+j} a - \left(\frac{\delta}{1+j} \right)^2 \right) \right] \\
&= u_x \left[1 - \left(\frac{2}{1+j} \right) \frac{\delta}{a} + \frac{2}{(1+j)^2} \left(\frac{\delta}{a} \right)^2 \right] \\
&= u_x \left[1 - (1-j) \frac{\delta}{a} - j \left(\frac{\delta}{a} \right)^2 \right].
\end{aligned} \tag{86}$$

Ignoring the higher order term in equation (86), equation (83) becomes

$$z_m = \frac{f/\langle u \rangle_s}{\langle u \rangle_s} = \frac{m \frac{\partial u}{\partial t}}{\langle u \rangle_s} = \frac{j \omega m u_x}{u_x \left[1 - (1-j) \frac{\delta}{a} \right]} = \frac{\omega m \frac{\delta}{a}}{2 \left(\frac{\delta}{a} \right)^2 - 2 \frac{\delta}{a} + 1} - \frac{j \omega m \left(\frac{\delta}{a} - 1 \right)}{2 \left(\frac{\delta}{a} \right)^2 - 2 \frac{\delta}{a} + 1}. \tag{87}$$

Equation (87) can be linearized leading to a real part resistance, $R_m = \omega m \frac{\delta}{a}$, and an imaginary part reactance, $X_m = \omega m \left(1 + \frac{\delta}{a} \right)$.

Using the temporal absorption coefficient for a damped harmonic oscillator, $\beta = \frac{R_m}{2m}$, and the relationship $\alpha/k = \beta/\omega$, then

$$\alpha_{wm} = \beta/c = \frac{1}{2c} \omega \frac{\delta}{a} = \frac{1}{2ac} \omega \left(\frac{2v}{\omega} \right)^{1/2} = \frac{1}{ac} \left(\frac{v\omega}{2} \right)^{1/2}. \tag{88}$$

For an isothermal pipe wall, the loss through thermal conduction at the wall can also be written as

$$\alpha_{wk} = \frac{1}{ac} \left(\frac{v\omega}{2} \right)^{1/2} \frac{\gamma-1}{\sqrt{\text{Pr}}}. \tag{89}$$

This leads to a total loss at the wall of (ref. 9):

$$\alpha_{wk} = \alpha_{wm} + \alpha_{wk} = \frac{1}{ac} \left(\frac{v\omega}{2} \right)^{1/2} \left(1 + \frac{\gamma-1}{\sqrt{\text{Pr}}} \right). \tag{90}$$

4. MISCELLANEOUS

4.1 Justification for the Plane Wave Assumption

Shown here for this application, the use of a 1D plane wave equation is justified. In cylindrical coordinates (fig. 6), the wave equation can be written as

$$\left(\nabla^2 - \frac{1}{c^2} \frac{\partial^2}{\partial t^2} \right) p = 0, \quad (91)$$

with $\nabla^2 = \frac{\partial^2}{\partial r^2} + \frac{1}{r} \frac{\partial}{\partial r} + \frac{1}{r^2} \frac{\partial^2}{\partial \theta^2} + \frac{\partial^2}{\partial z^2}$. Using separation of variables, one can write

$$p = p(r, \theta, z, t) = R(r)\Theta(\theta)Z(z)e^{j\omega t}. \quad (92)$$

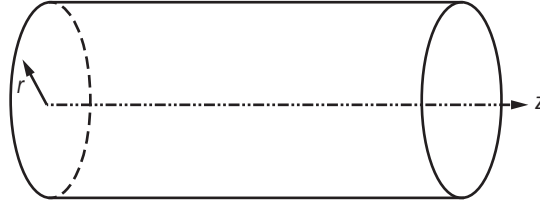


Figure 6. Coordinate system for a cylindrical port.

Let $\psi = R\Theta Z$, equation (90) becomes the Helmholtz equation:

$$\left(\nabla^2 + k^2 \right) \psi = 0. \quad (93)$$

with the boundary conditions at rigid walls

$$\left(\frac{\partial \psi}{\partial z} \right)_{z=L} = \left(\frac{\partial \psi}{\partial r} \right)_{r=a} = 0. \quad (94)$$

Separation of variables results in three equations:

$$\frac{1}{R} \left(\frac{\partial^2 R}{\partial r^2} + \frac{1}{r} \frac{\partial R}{\partial r} \right) + \frac{1}{r^2 \Theta} \frac{\partial^2 \Theta}{\partial \theta^2} + \frac{1}{Z} \frac{\partial^2 Z}{\partial z^2} + k^2 = 0, \quad (95)$$

$$\frac{\partial^2 Z}{\partial z^2} = -k_z^2 Z, \quad (96)$$

$$\frac{\partial^2 \Theta}{\partial \theta^2} = -m^2 \Theta, \quad (97)$$

and upon substitution into equation (93) becomes

$$r^2 \frac{\partial^2 R}{\partial r^2} + r \frac{\partial R}{\partial r} + (k_{ml}^2 r^2 - m^2) R = 0, \quad (98)$$

with $k^2 = k_{ml}^2 + k_z^2$.

The solution can be written as

$$p_{ml} = A_{ml} J_m(k_{ml} r) \cos m\theta e^{j(\omega t - k_z z)}, \quad (99)$$

$$\text{with } k_z = \left[\left(\frac{\omega}{c} \right)^2 - k_{ml}^2 \right]^{1/2}.$$

With $J_m(k_{ml} r)$ the m th order Bessel function, and the allowed k_{ml} are determined by the boundary condition at the rigid wall,

$$\left(\frac{\partial R}{\partial r} \right)_{r=a} = 0, \quad J'(k_{ml} a) = 0, \quad k_{ml} = \frac{j'_{ml}}{a}. \quad (100)$$

The (m, l) mode indicates the mode of the wave traveling in the z -direction, the $(0, 0)$ mode is a plane wave propagating with $c_p = c$ for all $\omega > 0$. For the $(1, 1)$ mode, $j'_{11} = 1.84$, so the frequency cutoff $f_{11} = 1.84c/2\pi a$. For frequencies below f_{11} , only plane waves can propagate in a rigid-walled cylindrical wave guide. As an example, if $a = 0.25$ inch $= 6.35 \times 10^{-3}$ m, then $f_{11} = 1.84 * 340 / 2\pi a = 1.568 \times 10^4$ Hz, or $\lambda = 2\pi/k = 2\pi a / 1.84 = 3.41a = 0.022$ m. That is, if the frequency is lower than 1.568×10^4 Hz, or the wavelength greater than 0.022 m, the wave traveling in the z direction is a plane wave. Rayleigh¹⁰ has shown that a wave must eventually become a plane wave if the frequency is lower than the lowest natural transverse frequency. For a cylindrical tube, it is $\lambda > 3.41a$. If the highest frequency is

$f_{1r} = 1 \times 10^4$ Hz, the plane wave assumption is valid for a tube radius $a < 0.392$ inch in air at ambient conditions. With $a = 0.25$ inch, the experiment in this TP satisfies this condition.

4.2 Pressure Measurement Locations

It is proposed that the dynamic pressure measurement sampling location should be chosen on the end cap instead of the side wall. Tijdeman¹¹ summarized prior studies on the propagation of sound waves in cylindrical pipes. He concluded that the shear wave number, $s = \sqrt{2}a / \delta$, and reduced frequency, $k = \omega a / c_0$ are the two main parameters governing the propagation of sound waves. His plots of velocity distributions in an infinite tube show that the approximation of plane wave is justified when $s > 20$. For air at standard conditions ($T = 300$ K, $p = 1$ atm), and if the pipe diameter is 0.5 inch as in the experiment, then

$$\begin{aligned} s &\approx 13, \text{ when } f = 10 \text{ Hz,} \\ s &\approx 40, \text{ when } f = 100 \text{ Hz,} \\ s &\approx 127, \text{ when } f = 1,000 \text{ Hz,} \end{aligned}$$

and

$$s \approx 179, \text{ when } f = 2,000 \text{ Hz.}$$

The definition of the shear wave number, $s = \sqrt{2}a / \delta$, actually indicates whether a wide pipe approximation is appropriate. These calculations indicate this condition is satisfied for frequency as low as 25 Hz in the discussed port experiments. From figure 7, it can also be shown that on the wall, the velocity (or acoustic pressure) cannot be the best representation of the cross-section average; therefore, the best pressure sampling location should not be on the side wall.

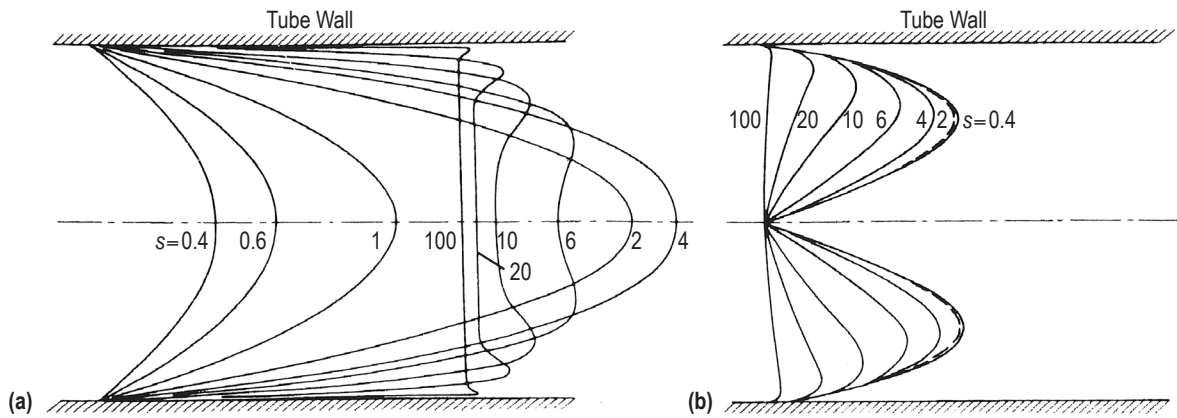


Figure 7. Tube wall—velocity distribution in (a) axial direction and (b) radial direction.

Furthermore, plane acoustic waves propagating in a rigid end-capped tube result in standing waves, as illustrated in figure 8. If a microphone is placed at the pressure node position, the output will be minimized. If the measured frequency is known, then the microphone position can be carefully calculated to avoid a pressure node. For broadband sound waves, a position on the side wall will inescapably fall to the pressure nodes for some frequencies.

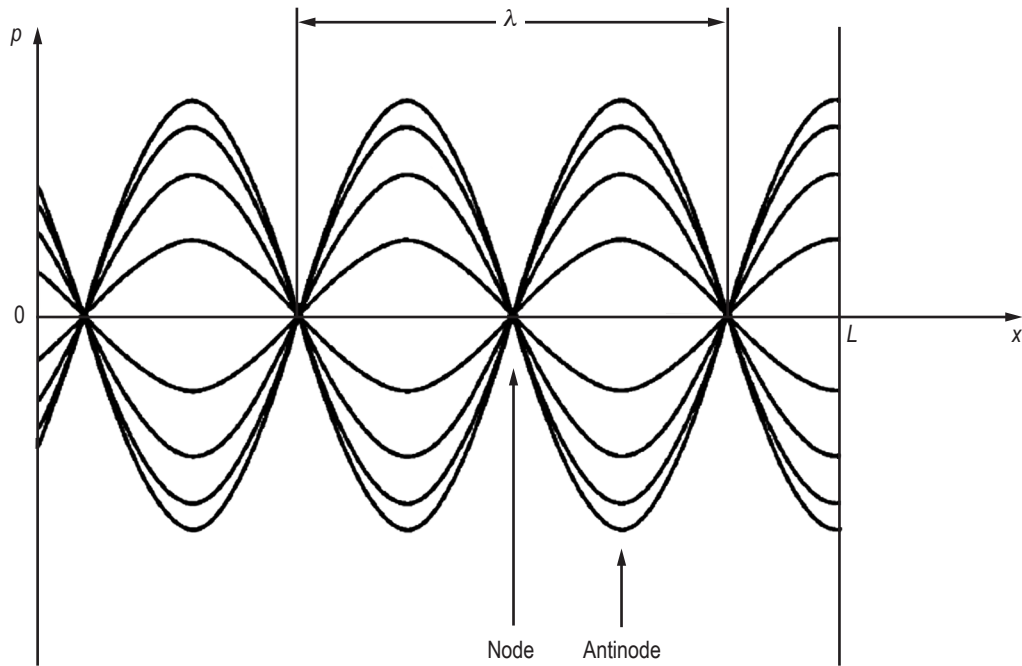


Figure 8. Display of standing wave node and antinode.

5. RESULTS

5.1 Experimental Results

Two sets of experiments were conducted—an experiment using a PVC pipe and an experiment using a large aluminum plate with different size cavities representing sensor ports. Data are represented as sound pressure level (SPL) spectrum plots in this TP where

$$\text{SPL}=20 \cdot \log_{10} \left(\frac{P_e}{P_{\text{ref}}} \right) \quad (101)$$

and the reference pressure, P_{ref} , is for air equal to 20×10^{-6} Pa. All spectra in this TP have a frequency resolution of 8 Hz unless otherwise noted.

5.1.1 Experiment Using a PVC Pipe

The PVC pipe experiment was designed to help test the analytical model early in the project. The idea was to send plane acoustic waves normal to the pipe entrance and make two acoustic pressure measurements—one at the inlet of the pipe and the other at the back end of the pipe which was closed. Figure 9 shows the setup used—a plane wave speaker on the floor of the anechoic chamber, a vertical PVC pipe held in place by a tripod holder. The top end of the pipe is closed by a 0.5-inch B&K microphone embedded in a spongy disk that fits tightly in the pipe. The dimensions of the pipe were 18.625 inches long with a 2.5-inch microphone insert area, leaving 16.125 inches in free length for the acoustic waves to travel. The pipe has a 1.6-inch inner diameter and is 0.16 inch thick.

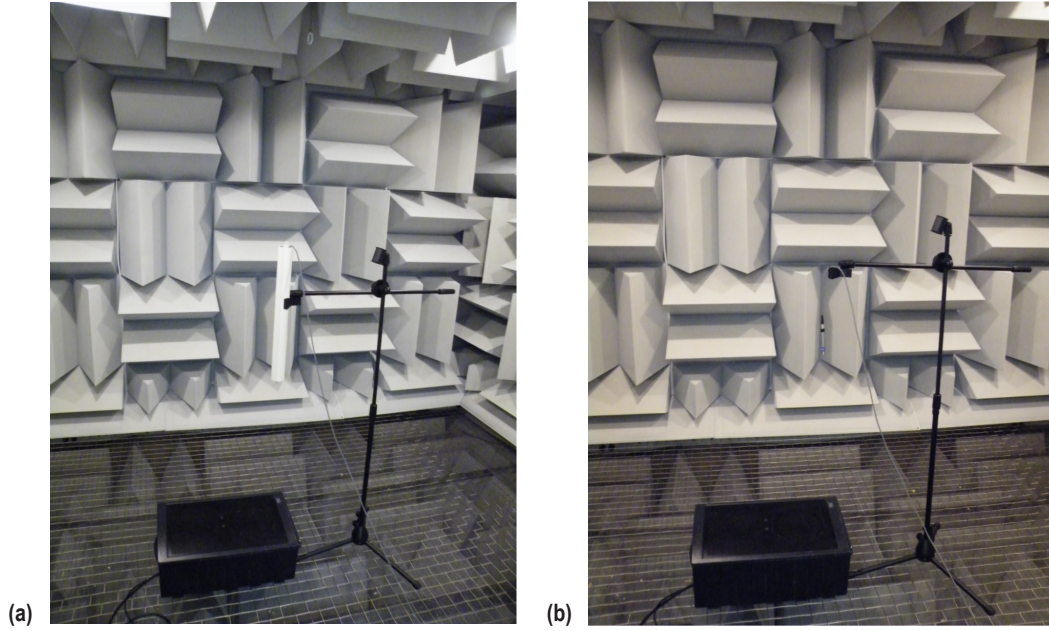


Figure 9. Setup for the PVC pipe experiment: (a) Measured at the top of the pipe and (b) incident wave measurement.

Figure 10 shows the time history of the measured acoustic pressure at the end of the PVC pipe and at the inlet of the pipe, as well as at the inlet location without the pipe present. The amplitude of the acoustic pressure at the end of the pipe is much larger than that at the inlet with or without the pipe. It is also observed that there is an effect of the pipe on the inlet pressure time history amplitude. The presence of the pipe increases the amplitude (green line).

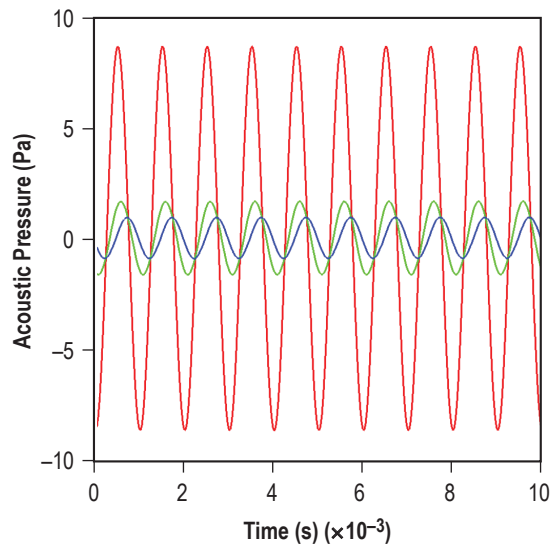


Figure 10. Time history of the acoustic pressure at the end of the PVC pipe (red line), at the inlet of the pipe (green line), and at the inlet location without the pipe present (blue line).

5.1.2 Experiment Using a Plate With Sensor Port Cavities

This experiment is the core of this project. Starting from one of the plates shown in figure 11, careful design and machining was carried out to arrive at the finished plate ready to test (fig. 12).



Figure 11. A pile of aluminum plates at Marshall Space Flight Center, one of which was used in the test.

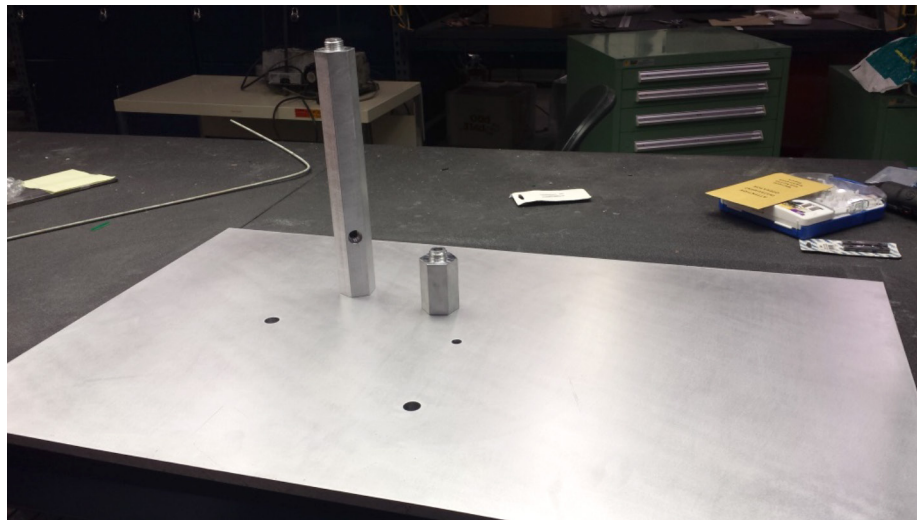


Figure 12. Finished aluminum plate with sensor ports ready to test.

Figure 12 shows the finished plate with sensor housings machined and the surface polished. Also shown in figure 12 are the short and long ports used in the test to simulate a recessed sensor port. The short and long ports were machined out of a hexagonal-shaped aluminum bar. The short port including plate recess is 2.991 inches long. The diameter of the sensor port drilled was 0.5 inch, matching the diameter of the B&K microphone diaphragm. The long port is 13.244 inches long and was used to allow for two sidewall measurements along the port in addition to the measurement at the end of the port. These additional measurement locations will allow for model validation. Two other larger holes visible on the figure are used as ‘witness’ ports used to house additional sensors. The conceptual design for the plate experiment is shown in figure 13, with (a) the plate top view and (b) the side view showing three sensors in the port and one sensor in the plate. Figures 14–16 show the as-built dimensions of the plate, short port, and long port, respectively. The as-built dimensions take into account the machining difficulties and accuracies. These dimensions are used to test the models and the computational results. All dimensions in the figures are in inches.

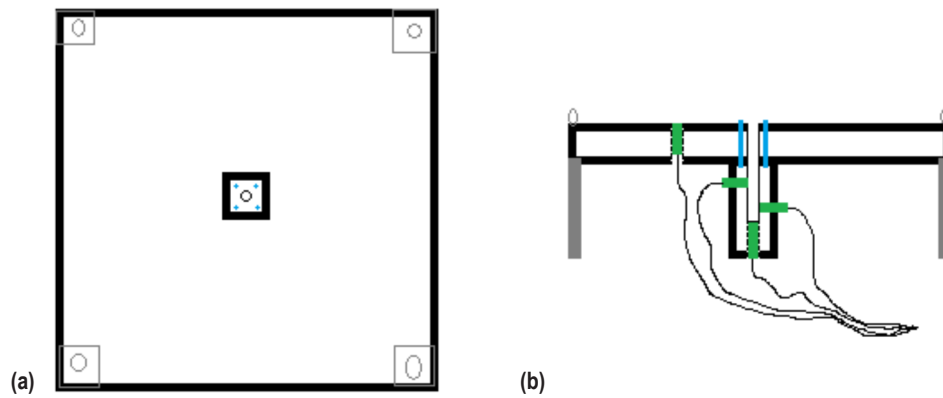


Figure 13. Schematic of the plate experiment: (a) Top view and (b) side view.

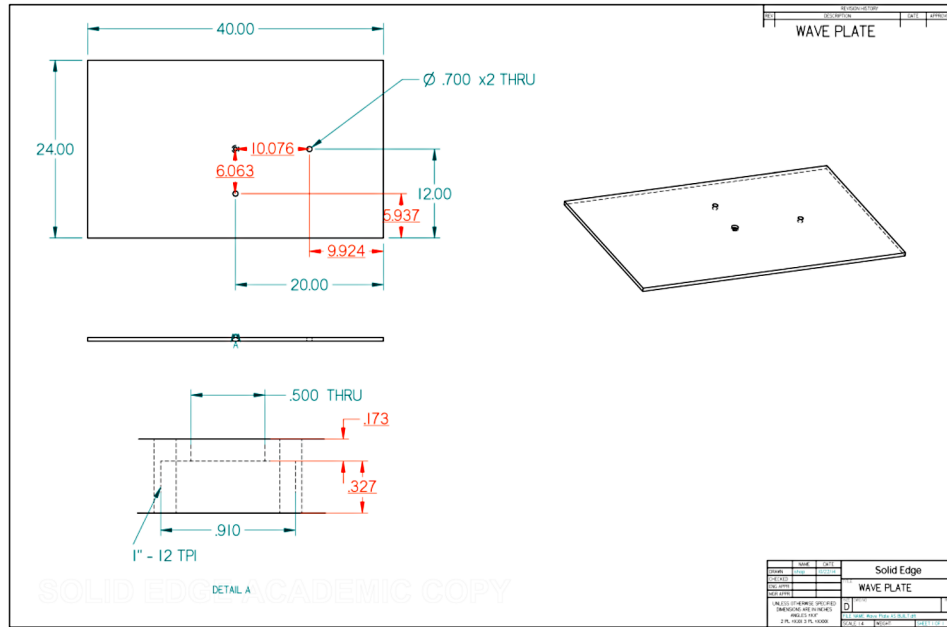


Figure 14. The as-built dimensions of the plate and sensor ports.

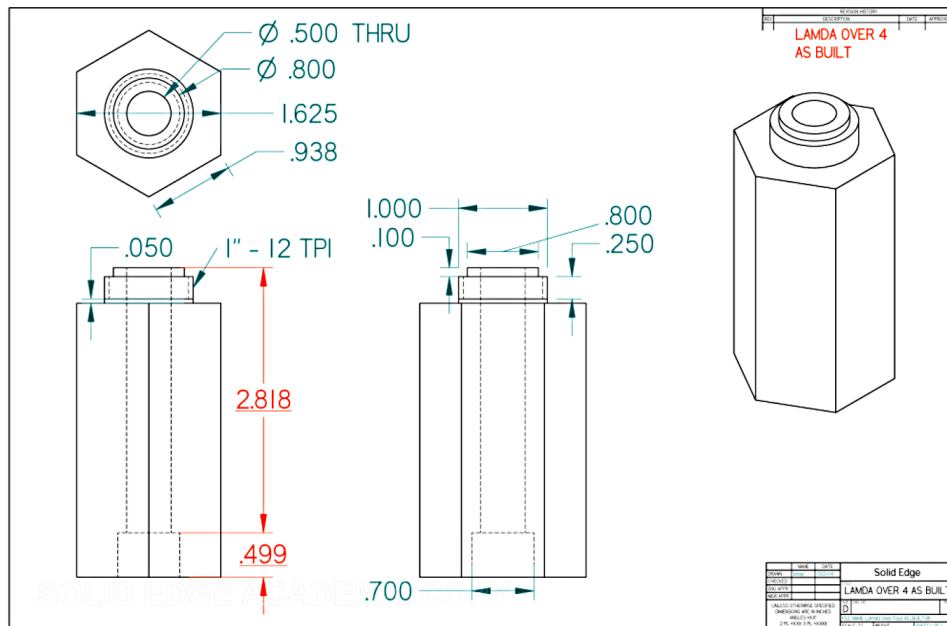


Figure 15. The as-built dimensions of the short port.

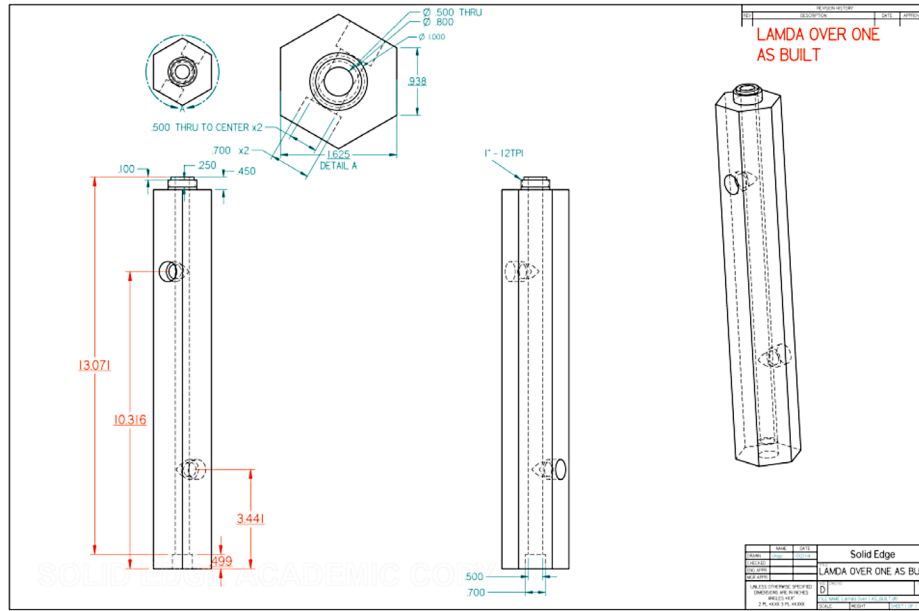


Figure 16. The as-built dimensions of the long port.

Figure 17 shows the experimental setup for the plate experiment in the anechoic chamber. In figure 17(a), a short port is shown attached to the plate. Also shown are three 0.5-inch microphones installed in the various ports to measure the acoustic pressure. In figure 17(b), the plane wave speaker is placed flat on the chamber floor and the plate is suspended from the ceiling using bungee cords with its leading edge just above the speaker. Figure 18 shows the various components used to carry out the experiment. The Pulse software by B&K is used to set up the type of signal generated—harmonic, random, or sweep—and to collect data as needed. The software allows real-time postprocessing such as fast Fourier transforms, power spectral densities (PSDs), and time histories. The various graphs generated can be saved and exported into a document created within the Pulse software.

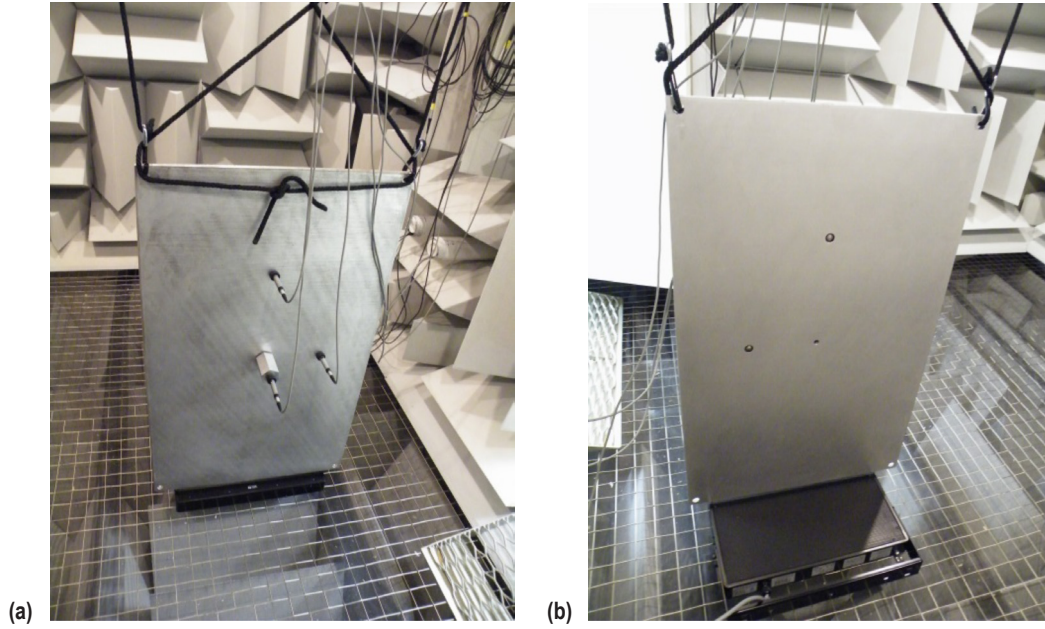


Figure 17. Suspended plate: (a) Rear view with microphones and (b) front view with the plane wave speaker.

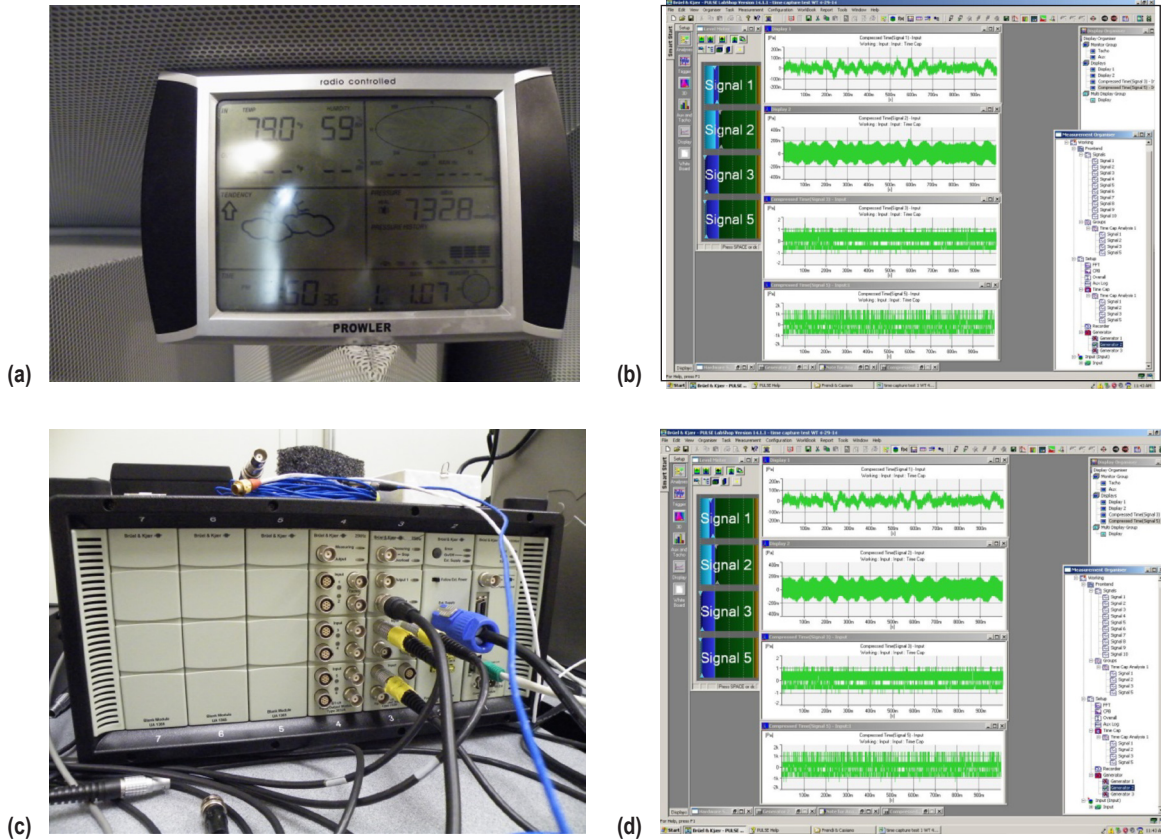


Figure 18. Various components used in the experiments: (a) Temperature and humidity measurement, (b) amplifier used, (c) the pulse system input-output, and (d) the Pulse software screen display.

5.1.2.1 Experimental Results for the Short Port. Several tests were conducted with a short port (length of 2.991 inches). A cartoon is shown in figure 19 showing microphone locations. The parameter that was varied during these tests was the frequency of the incident plane acoustic waves. At first, a harmonic plane acoustic wave of 1,000 Hz frequency was used. At this frequency, and according to design, the short port cavity should resonate at its quarter wave mode. Pressure data were acquired from four 0.5-inch-diameter microphones at various locations on the plate and in the port. In the following discussion, mic1 is the microphone at the end of the short port located at the center of the plate 20 inches from the leading edge, mic2 is the microphone on the plate 20 inches from the leading edge and 6.063 inches off-center, and mic3 is the microphone 10.076 inches downstream of the plate center. The time history of the acoustic pressure at the three microphone locations is shown in figure 20. It is clear from the figure that mic1 pressure exhibits an amplitude nearly 40 times larger than that of mic2 and mic3. This indicates that the 1,000 Hz frequency is in the proximity of the resonance frequency of the short port.

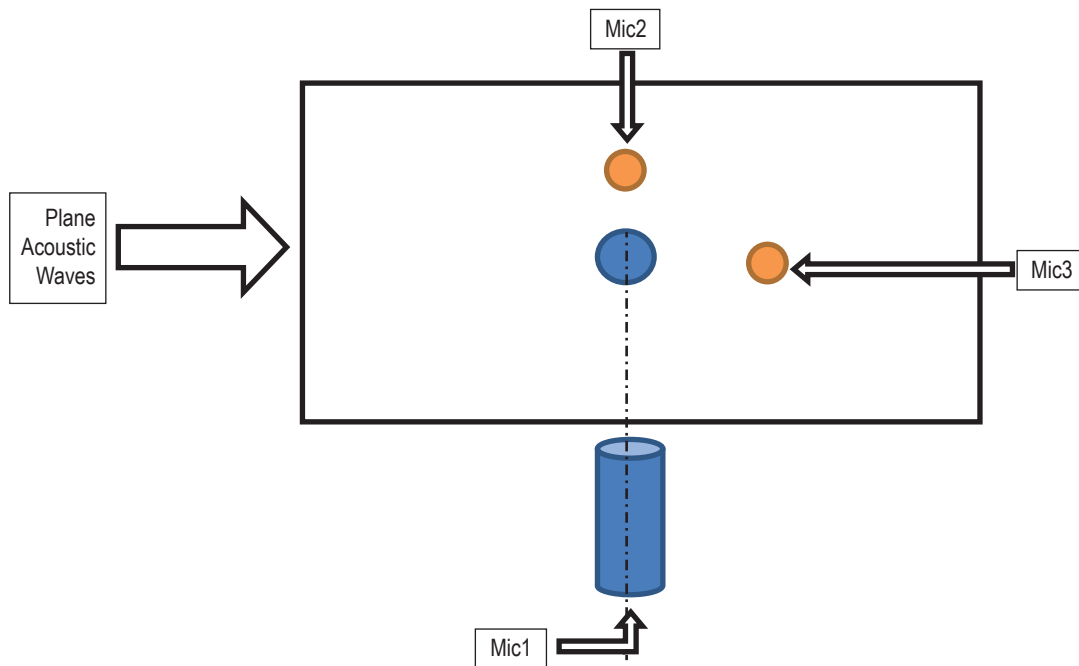


Figure 19. Microphone locations on short port configuration.

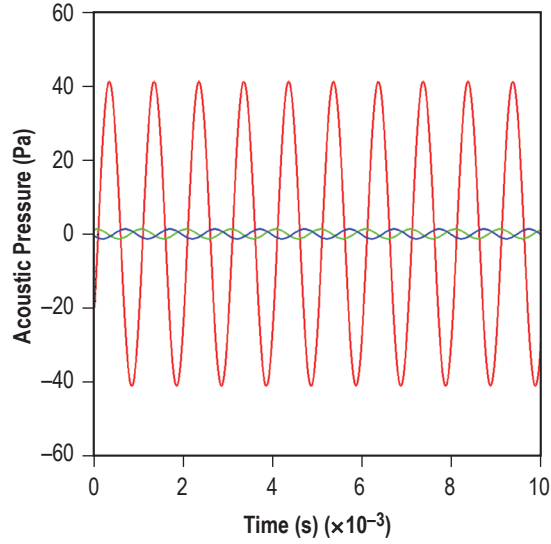


Figure 20. Time history of the acoustic pressure at mic1 (red), mic2 (green), and mic3 (blue) at 1,000 Hz.

Figure 21 shows the SPL spectrum at the three microphone locations, with mic1 showing the highest SPL at the 1,000 Hz frequency. There is nearly a 30 dB difference in the level between mic1 and mic2 and no significant difference between mic2 and mic3. In addition to the 1,000 Hz peak in the SPL spectrum plots, weaker 2,000, 3,000, and 4,000 Hz peaks are also shown. These frequency peaks are harmonics of the fundamental frequency of 1,000 Hz and are present due to imperfect representation of a pure sinusoid. In addition to the 1,000 Hz frequency used above, other frequencies were also applied; namely, 500, 750, and 1,500 Hz. Figure 22 shows the pressure time histories at the three microphone locations for these three plane wave frequencies. Of the additional frequencies, the amplitude of mic1 pressure is highest at 750 Hz as it is the closest to the resonance frequency of 1,000 Hz. The phase relationship between the three measurement locations changes with frequency as the figure shows.

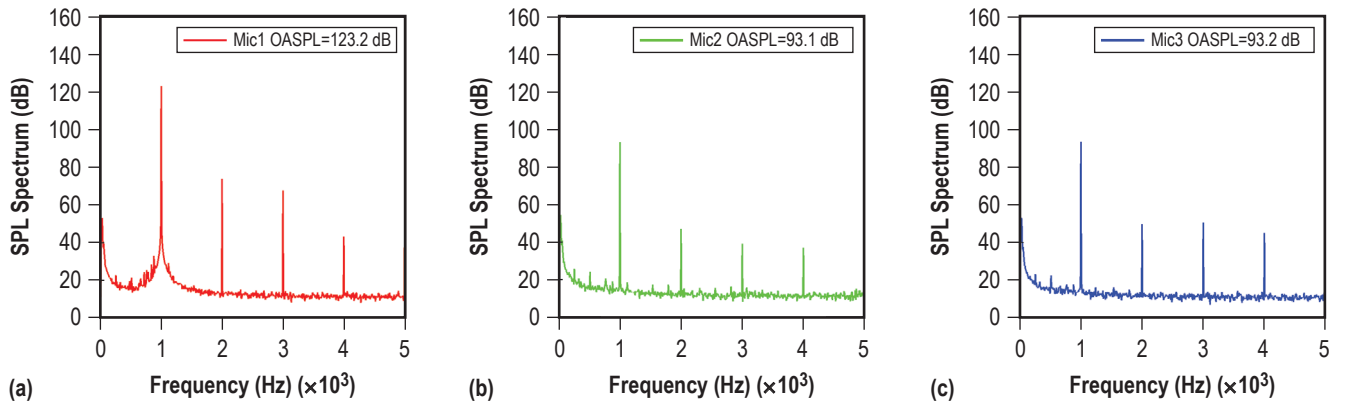


Figure 21. SPL spectrum at various microphone locations: (a) mic1, (b) mic2, and (c) mic3.

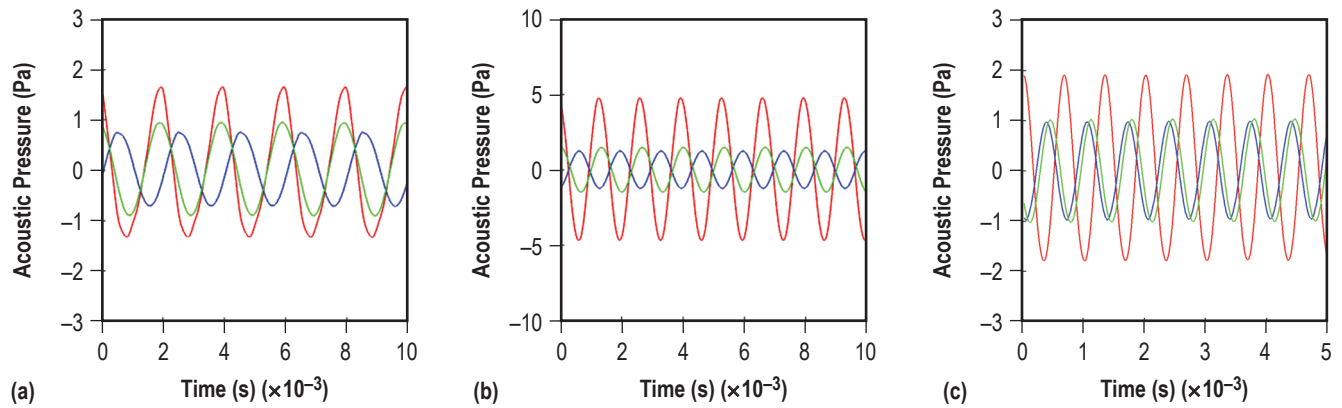


Figure 22. Time history of the acoustic pressure measured at mic1 (red), mic2 (green), and mic3 (blue), and at three different frequencies: (a) 500 Hz, (b) 750 Hz, and (c) 1,500 Hz.

A frequency sweep test was performed to check the response of the short port. Figure 23 shows (a) the time history of the acoustic pressure, (b) the frequency, and (c) the acoustic pressure peak amplitude. Both the (a) and (c) plots show the presence of one strong resonant frequency near to 1,000 Hz. In fact, the peak amplitude is slightly less than 1,000 Hz and reaches 60 psi from a 1 psi excitation. This shows the actual quarter wave resonance occurs at 980 Hz.

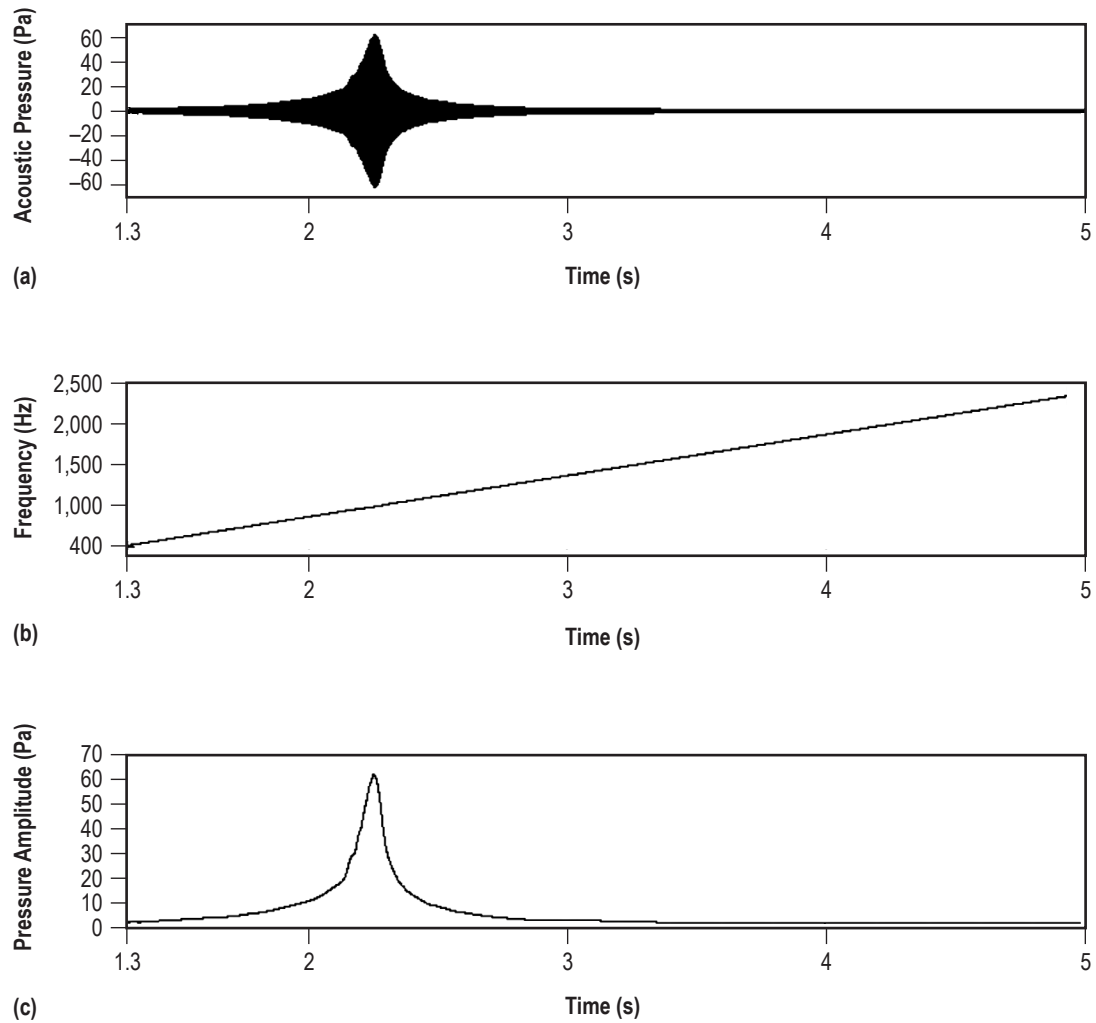


Figure 23. Response of a short port to a frequency sweep—mic1: (a) Acoustic pressure time history, (b) frequency, and (c) instantaneous pressure peak amplitude.

Certainly the most important test with broad engineering applications is the test that subjects the short port to a broadband frequency excitation, also known as white noise. The importance of this stems from the fact that most engineering applications are highly random in nature with broad frequency content. Such applications include rocket engine combustion chamber flow and turbulent boundary layer flow. It is also able to establish information over a full bandwidth. Figure 24 shows the time history of the acoustic pressure at mic1, mic2, and mic3. The acoustic pressure at mic1 exhibits large amplitude random fluctuations (red line), whereas the pressure fluctuations at mic2 and mic3 are of similar lower amplitudes (green and blue lines, respectively).

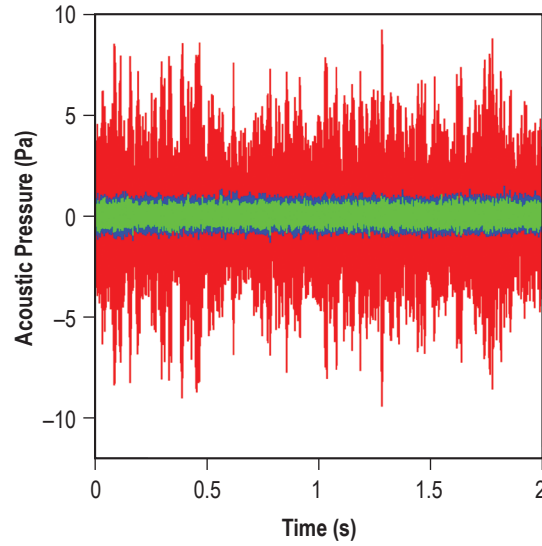


Figure 24. Time history of acoustic pressure at mic1 (red), mic2 (green), and mic3 (blue) driven from white noise.

Figure 25 shows the SPL spectrum of the acoustic pressure at the three locations—mic1, mic2, and mic3. The mic1 SPL spectrum shows a strong peak near 1,000 Hz and a weaker peak near 3,000 Hz, whereas mic2 and mic3 show a broadband spectrum as expected. Figure 26 shows the transfer function between mic1 and mic3. A large peak near 1,000 Hz is obtained with a smaller peak at 3,000 Hz.

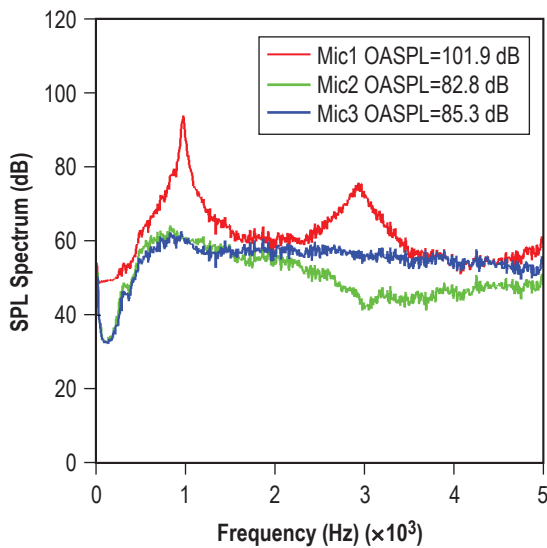


Figure 25. SPL spectrum of acoustic pressure.

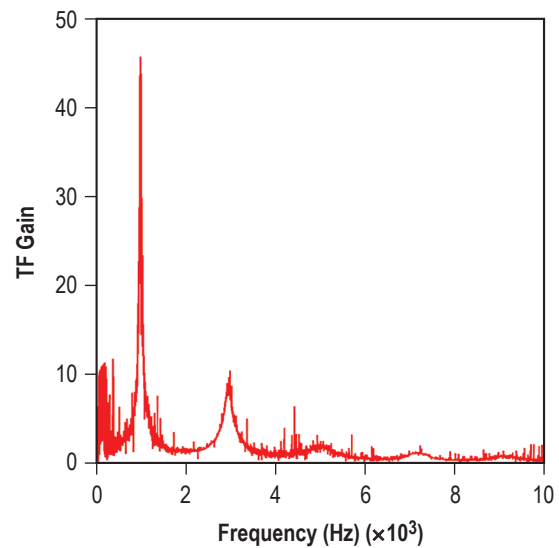


Figure 26. Transfer function between mic1 and mic3 for a random frequency plane wave.

5.1.2.2 Experimental Results for the Long Port. The long port, which is 13.244 inches, is used to provide more experimental results for analytical model validation. In addition to the three microphones used in the short port experiment, two more microphones are added along the port: mic4 at a distance of 3.427 inches from the plate surface and mic5 at a distance of 10.302 inches from the plate surface. Figure 27 shows microphone locations for the long port configuration. Since the quarter wave resonant frequency is no longer 1,000 Hz, the random plane wave frequency will be presented first in this section. Figure 28 shows the time history of the acoustic pressure at all microphone locations. The amplitude of the pressure in the port at mic1 (red), mic4 (light blue), and mic5 (purple) is the largest, as expected, whereas mic2 (green) and mic3 (deep blue) show pressure fluctuations of similar amplitudes. The SPL spectrum at mic1, mic2, and mic3 are shown in figure 29(a). The mic1 SPL spectrum shows a number of prominent peaks. The peaks occur at the resonance frequencies of the port, which are 245, 730, 1,234, 1,730, 2,195, 2,645, 3,225, and 3,730 Hz. Similar to figure 25, mic3 shows the broadband random input spectrum and is used as a reference for the transfer function computation. Comparison of mic4 SPL spectrum to that of mic3 shows a number of peaks at the mic4 location (fig. 29(b)), which is inside the port closer to the plate. There are deep valleys in the SPL spectrum of mic4, indicative of the absence of some frequencies in the spectrum at this location. The same can be said about the SPL spectrum of mic5 (fig. 29(c)), where some peaks are weaker and others are broader or just absent altogether.

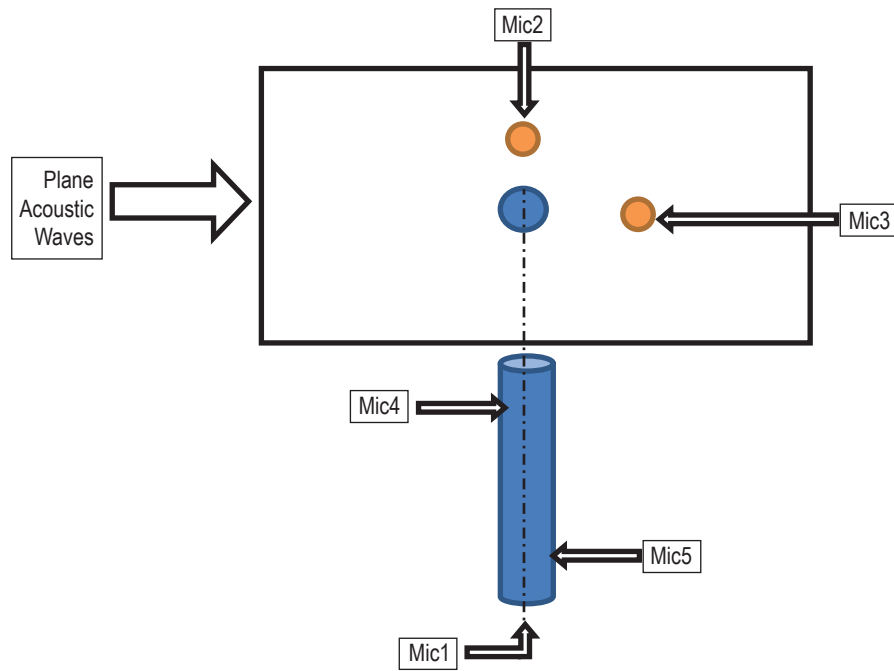


Figure 27. Microphone locations on long port configuration.

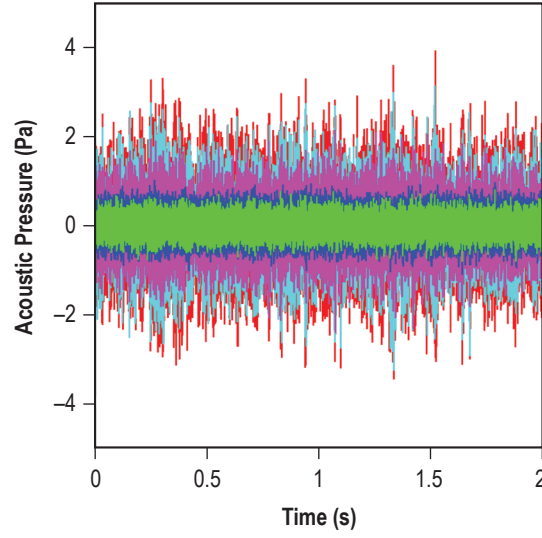


Figure 28. Time history of acoustic pressure at mic1 (red), mic2 (green), mic3 (deep blue), mic4 (light blue), and mic5 (purple) for the long port.

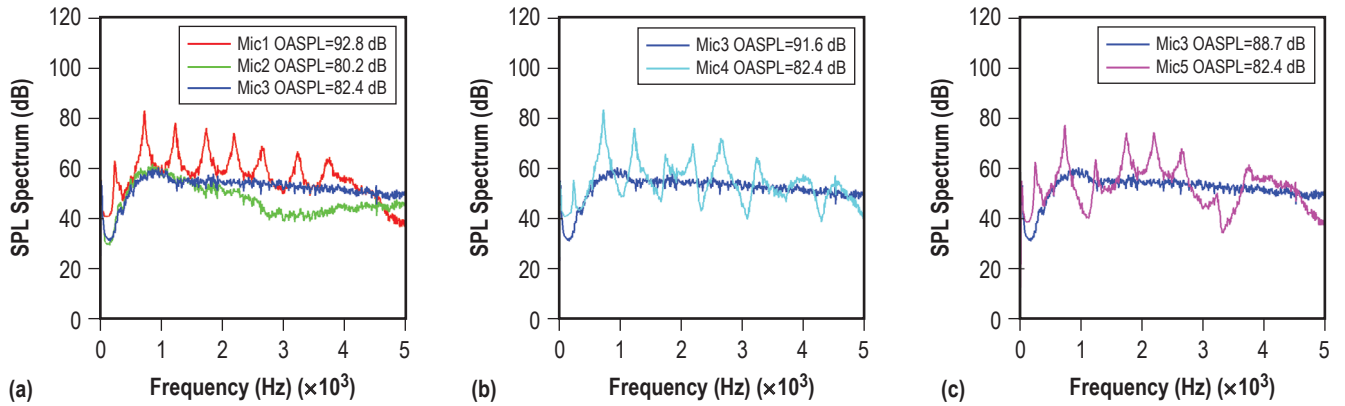


Figure 29. SPL spectrum of the pressure at (a) mic1, mic2, and mic3; (b) mic3 and mic4; and (c) mic3 and mic5.

The transfer function between mic1 and mic3, mic4 and mic3, and mic5 and mic3 are shown in figure 30. The transfer function between mic1 and mic3 (fig. 30(a)) exhibits several peaks with decreasing amplitude as the frequency increases; the highest peak at a frequency of 245 Hz, the quarter wave mode of the port. The transfer function between mic4 and mic3 (fig. 30(b)) also shows several peaks; however, the highest peak is at a frequency of 730 Hz.

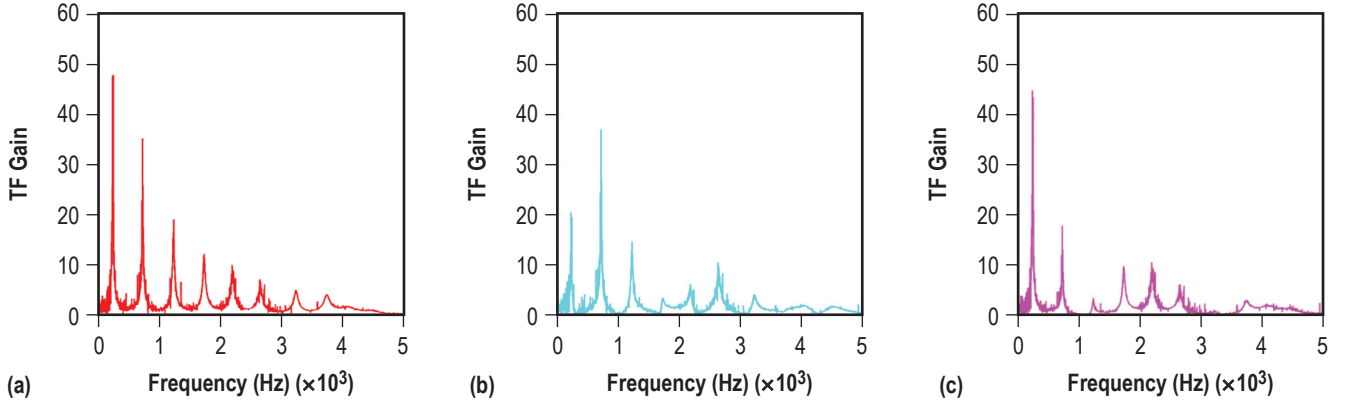


Figure 30. Transfer functions between (a) mic1 and mic3, (b) mic4 and mic3, and (c) mic5 and mic3.

Also worth noticing is that some of the frequencies present at mic1 in the back end of the port are weak or absent at mic4 within the port: 1,730 and 2,195 Hz. Similar to mic4, mic5 also shows some frequencies to be weak or absent: 1,234 and 2,645 Hz. These data are indicative of the spatial dependence of each mode. The fundamental quarter wave mode occurs at 245 Hz. The highest amplitude of the quarter wave mode is also obtained for the mic1 location in the back end of the port.

The frequency sweep test results are shown in figure 31. The time history of the pressure shows four blossoms of varying amplitudes corresponding to the various resonances shown in figure 29. The first blossom shown is actually the first harmonic and not the fundamental mode. Figure 31(b) shows the sweep frequency, and plots (c)–(e) show the peak pressure amplitude at the various locations, mic1, mic4, and mic5, respectively. The pressure amplitude at mic1 and mic4 is of similar maximum magnitude for the first frequency peak but differs at the other peaks. The pressure amplitude at mic5 is lower at all peaks.

In addition to the random and frequency sweep tests, harmonic plane waves of varying frequencies are used in the long port case. In particular, acoustic waves at frequencies of 500, 750, 1,000, and 1,500 Hz were generated. Figure 32 shows the comparison between mic1 and mic3 at these four frequencies. The highest peak of the comparison occurs at (b) a frequency of 750 Hz. The comparisons for mic4 and mic3 and mic5 and mic3 are shown in figures 33 and 34, respectively, for completeness. At all frequencies tested, the comparisons between mic5 and mic3 exhibits the highest amplitudes after those of mic1, which is to be expected since mic1 and mic5 are in close proximity to each other.

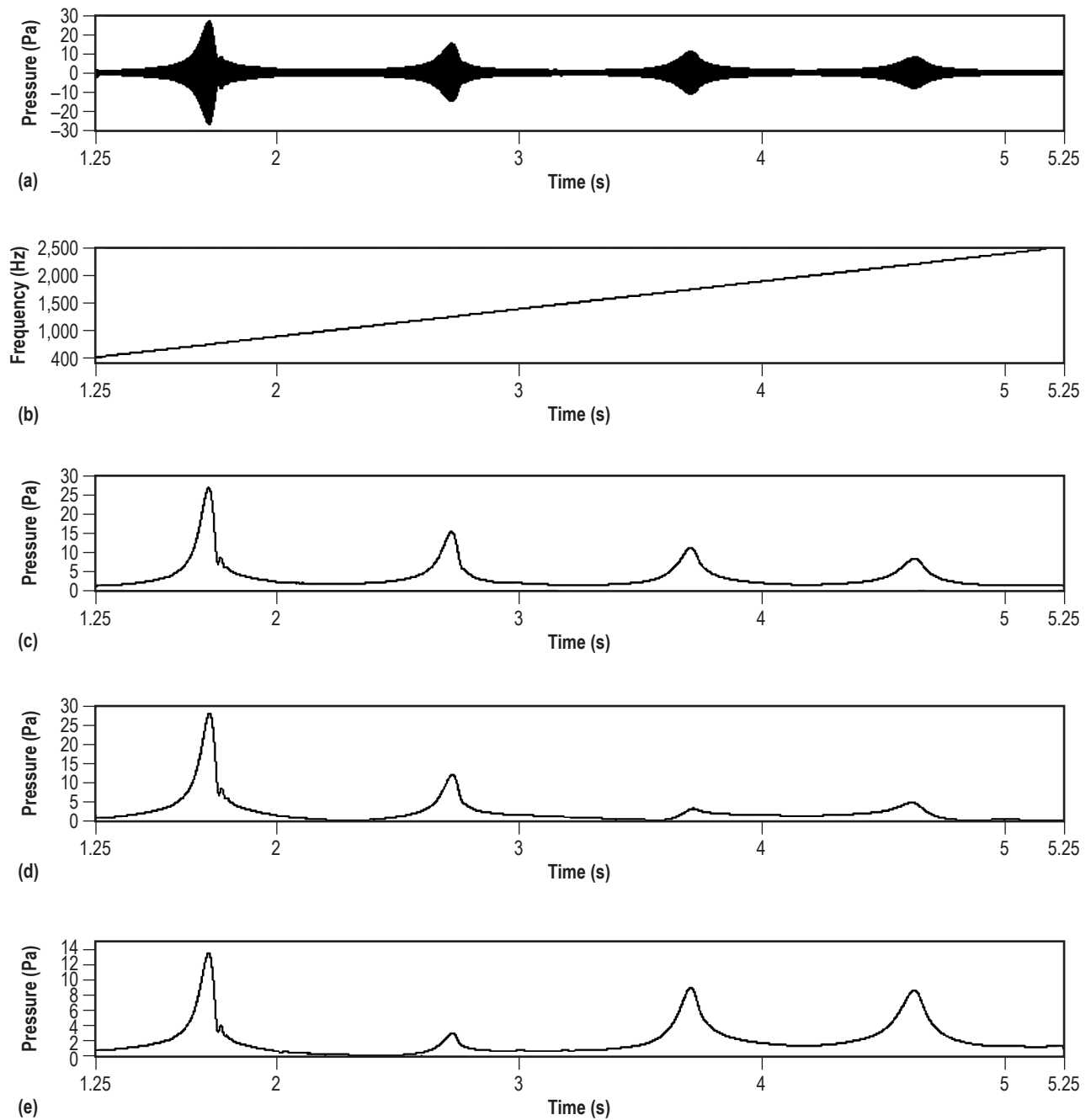


Figure 31. Response of the long port to a frequency sweep: (a) Acoustic pressure at mic1, (b) frequency, (c) instantaneous pressure peak amplitude at mic1, (d) instantaneous pressure peak amplitude at mic4, and (e) instantaneous pressure peak amplitude at mic5.

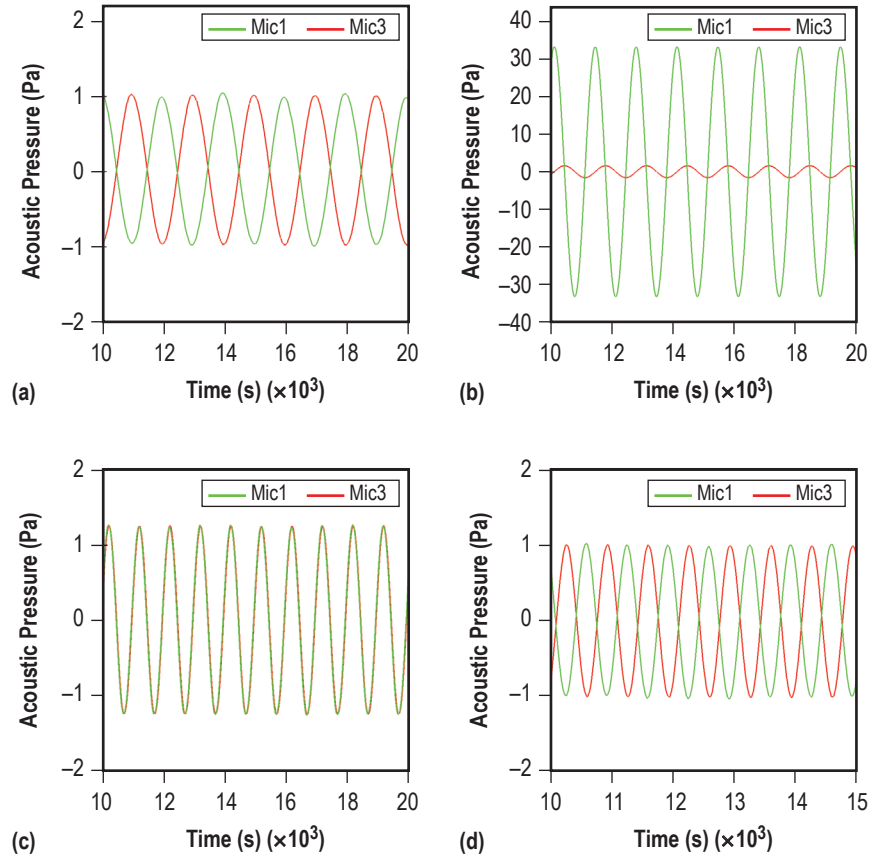


Figure 32. Comparison of mic1 and mic3 at (a) 500 Hz, (b) 750 Hz, (c) 1,000 Hz, and (d) 1,500 Hz.

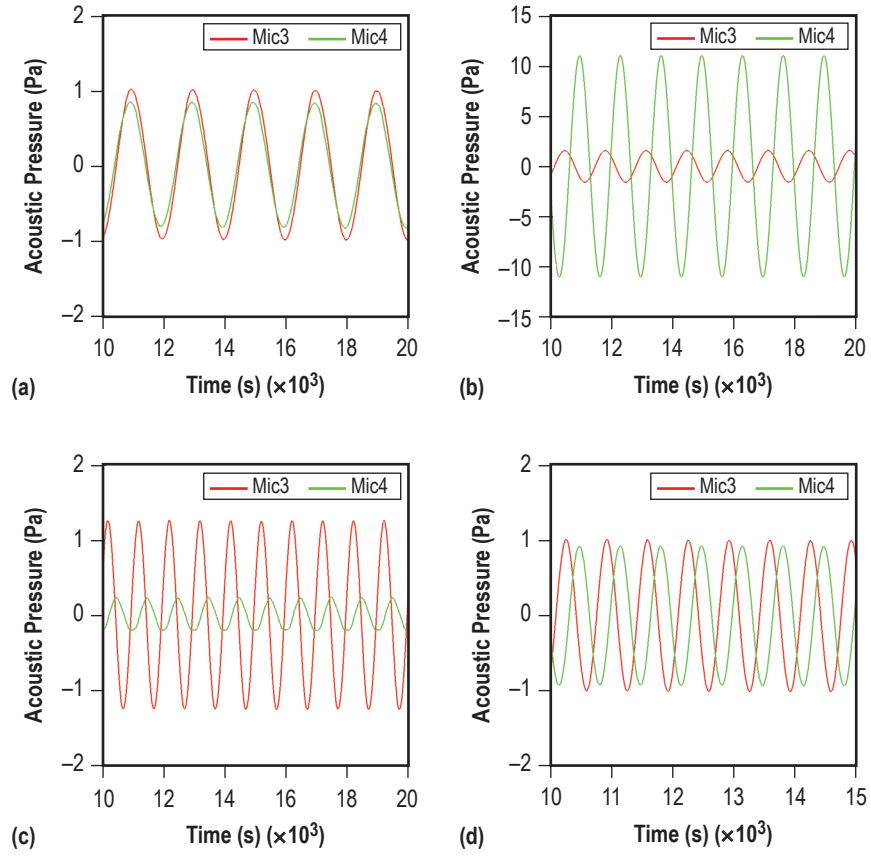


Figure 33. Comparison of mic4 and mic3 at (a) 500 Hz, (b) 750 Hz, (c) 1,000 Hz, and (d) 1,500 Hz.

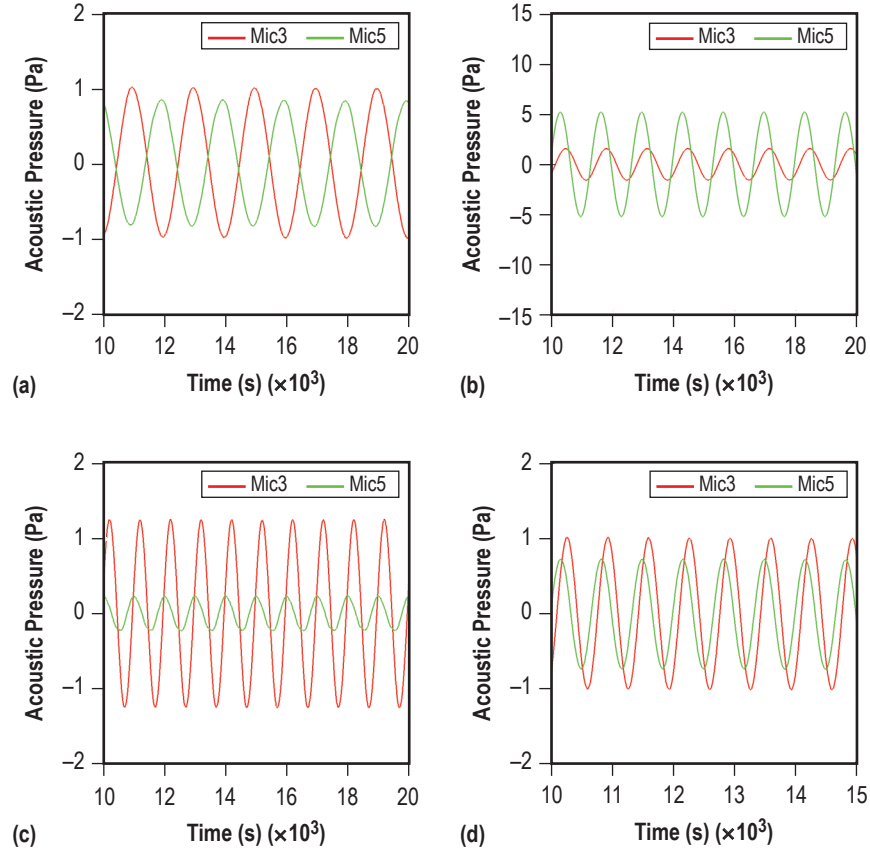


Figure 34. Comparison of mic5 and mic3 at (a) 500 Hz, (b) 750 Hz, (c) 1,000 Hz, and (d) 1,500 Hz.

5.2 Comparison of the Analytical Model Prediction to the Experimental Data

Before presenting the results, it is important to restate the motivation and the desired output from the developed model. When testing rocket engines, flush-mounted pressure measurements are needed in the combustion chamber to aid in the diagnostics of combustion instabilities, but because of the high temperature environment, these measurements are not always possible. Therefore, sensor ports that are recessed from the chamber are used to make such measurements; however, the question then arises as to how representative this measurement is to the desired measurement near the chamber wall, i.e., inlet of the sensor port. The model was developed to help an experimentalist determine a pressure at the inlet of a sensor port given a measurement made at another location in the port, in this case, the rigid end of the port. Both the forward and backward predictions of the model will be tested as a verification, knowing that the model will be used most often in the backward prediction or reconstruction of the pressure signal at the port inlet. Long port based experimental absorption coefficients are used in the models for all experiments (short port and long port) because other data were not available at the time of calculation.

5.2.1 The Plate With Sensor Ports

5.2.1.1 The Plate With a Short Port. Comparison is made of the model forward predictions using the random excitation data based on mic2 and mic3 data to obtain results at the mic1 location in the port and then compared to the measured mic1 data. Figure 35 shows a comparison of the measured (blue) and predicted (red and green) SPL spectrum at mic1. The prediction results were obtained using the developed analytical model using input data from mic2 and mic3 measurements. The SPL spectrum for figure 35 random input shows very good agreement between the measured and predicted SPL spectrum.

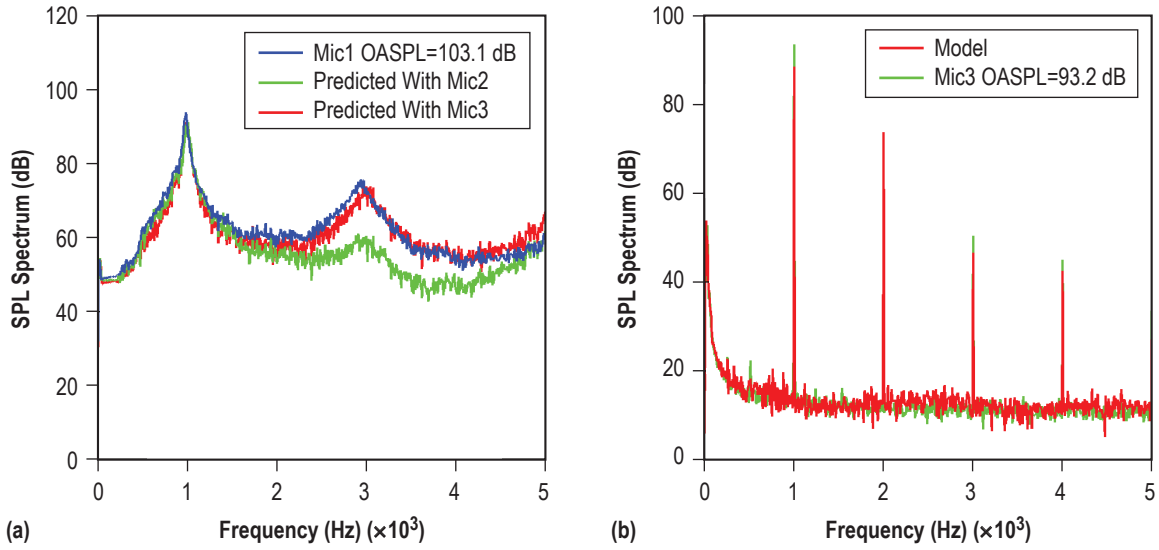


Figure 35. Measured and predicted SPL spectrum for plane wave input at mic1 location: (a) Random and (b) harmonic input at 1,000 Hz.

One of the key parameters in our prediction model is the spatial absorption coefficient, α . Using data from the long port for a random plane wave excitation to capture the most points since there are more modes and the PSD at mic1, the absorption coefficient can be calculated using the half-power method. Figure 36 shows the variation of the absorption coefficient with frequency. The predicted absorption coefficient is obtained from equation (90) while the measured absorption coefficient was obtained from the PSD of mic1 data using the half-power method. At low frequencies ($<1,500$ Hz), the predicted and measured absorption coefficient are in reasonably good agreement, whereas at higher frequencies, the predicted absorption coefficient is much lower than that measured. This is in part due to the fact that all the predicted model results presented in this TP are obtained using the experimental values of the absorption coefficient from the long port.

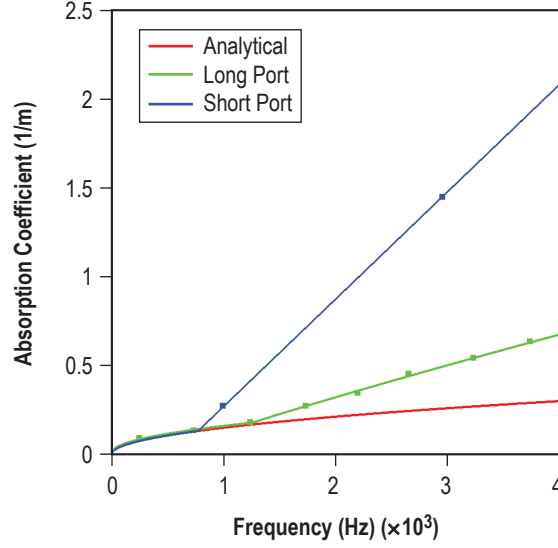


Figure 36. Absorption coefficient.

The half-power method consists of finding the peak center frequency, f_0 , with maximum power from a PSD, and then selecting the frequency above the peak, f_u , and below the peak, f_l , at the half-power level. The relation to absorption coefficient can then be found easily as follows. Quality factor is defined as

$$Q = \frac{f_0}{f_u - f_l}. \quad (102)$$

It can also be represented as a function of the temporal absorption coefficient, β , for a damped oscillator:

$$Q = \frac{\pi f_0}{\beta}. \quad (103)$$

The temporal absorption coefficient can be represented as the absorption coefficient by

$$\beta = \alpha \cdot c. \quad (104)$$

Equating equations (102) and (103) and substituting in equation (104) gives a relationship for the experimental based absorption coefficient, α_{exp} , that can be obtained from data:

$$\alpha_{\text{exp}} = \frac{\pi(f_u - f_l)}{c}. \quad (105)$$

The transfer function between predicted mic1 results and measured mic3 data are compared to the transfer function obtained using experimental data between mic1 and mic3 in figure 37 for random excitation. The plot shows a reasonably good agreement between the predicted and measured transfer function. The largest difference between the measured and predicted transfer function occurs at the 1,000 Hz frequency. Figures 35 and 37, obtained using the long port absorption coefficient from figure 36, show that this model is capable of producing reasonable results when exercised in the forward direction. The next test is to determine how the model performs in the backward direction, which is the direction of utmost importance for the intended application.

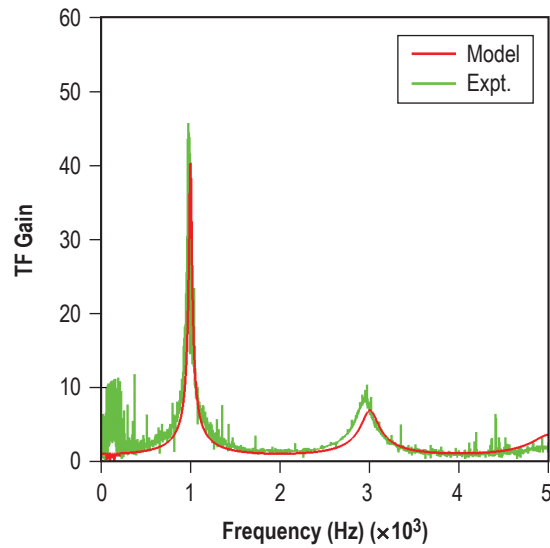


Figure 37. Transfer function gain at mic1 location.

Figure 38 shows the measured long port (green) and predicted (red) time history of the acoustic pressure at mic3 location for a random frequency plane wave input. The predicted pressure was obtained using mic1 experimental data and the long port experimental absorption coefficients. Overall good agreement is obtained between the measured data and predicted results. Comparison of the measured (green) and predicted (red) SPL at the mic3 location is given in figure 39. Once again, a reasonable agreement is obtained. Notice that the model predicts a larger decrease in SPL at higher frequencies. Harmonic plane wave inputs of different frequencies were also applied. Figure 40 shows the predicted (red) and measured (green) SPLs at the mic3 location using data from the mic1 location for the prediction. The model predicts frequency peaks in the spectrum reasonably well.

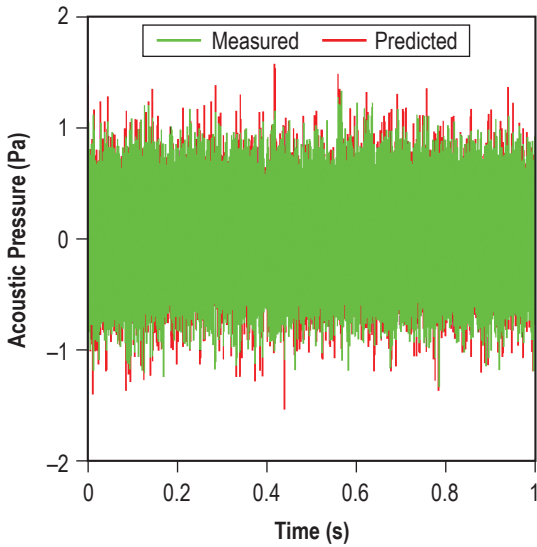


Figure 38. Time history of the pressure at mic3 location for a random frequency plane wave input.

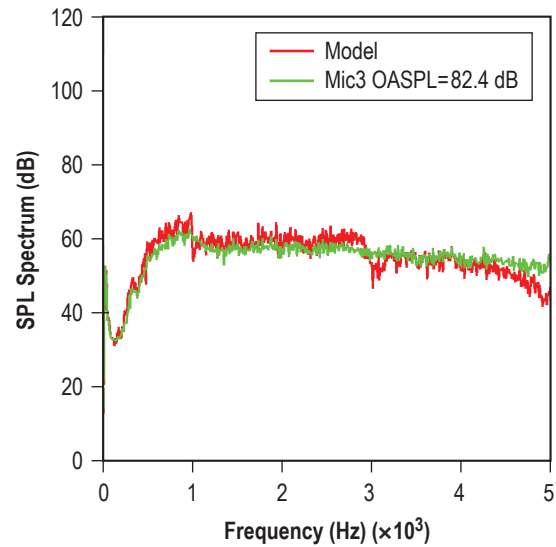


Figure 39. SPL spectrum at mic3 location for a random frequency plane wave input.

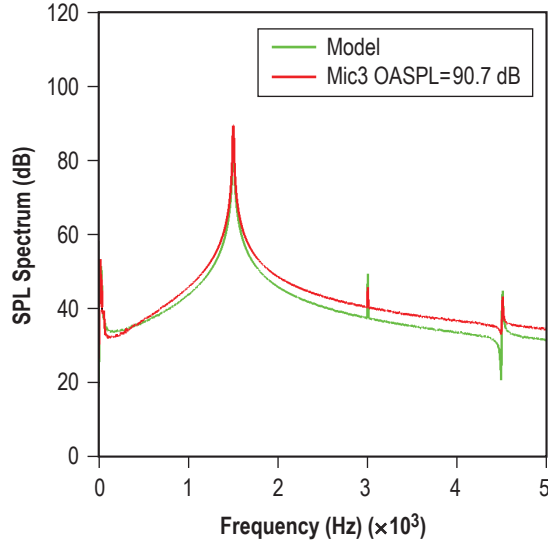


Figure 40. SPL spectrum at mic3 location using 1,500 Hz harmonic plane wave input.

5.2.1.2 The Plate With a Long Port. Similar to the short port results, the model is first tested in the forward direction. Figure 41 shows the measured (blue) and predicted (red and green) (a) SPL spectrum and (b) transfer function gain at the mic1 location for a random plane wave input. The (a) SPL spectrum results show good agreement with experimental data at frequencies lower than 4,000 Hz but overpredicts the level at higher frequencies. The (b) predicted transfer function from mic3 shows reduced amplitudes of the peaks at all frequencies with the biggest difference at the second resonance of 730 Hz. However, the ability of the model to predict all the peaks with reasonable accuracy is encouraging.

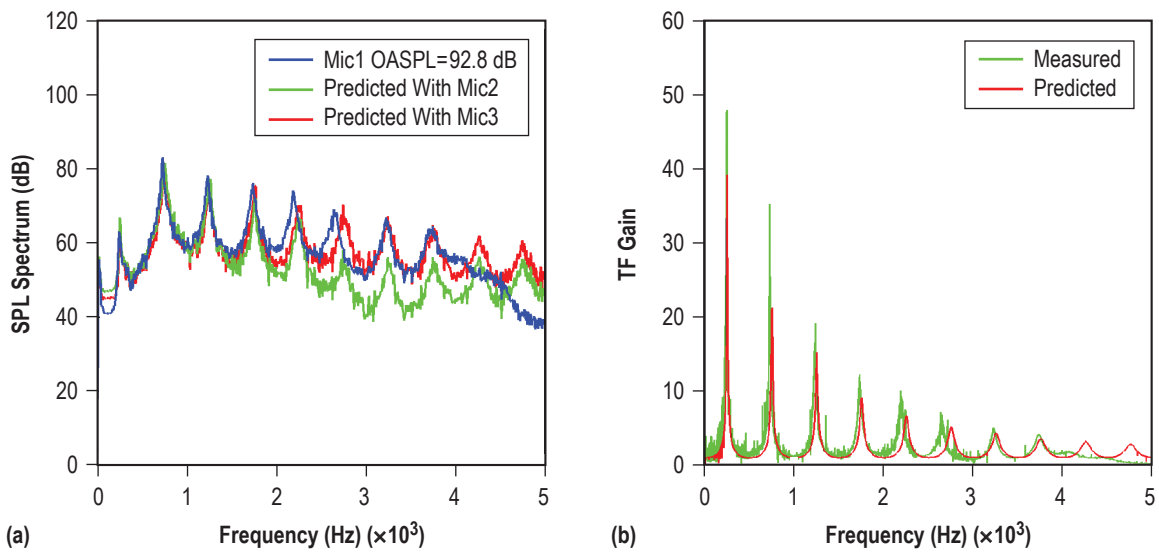


Figure 41. SPL spectrum at mic1 location for a random frequency plane wave input: (a) sound pressure level and (b) transfer function gain.

Next, the model is exercised in the reverse direction, i.e., using mic1 data to predict the mic3 location. For a random plane wave excitation, figure 42 shows the predicted time history of the pressure (red) at the mic3 location using mic1 data to have higher amplitude fluctuations than the measured data (plot (a)). This is verified with the SPL spectrum of the predicted pressure (plot (b)), which shows higher levels across the spectrum.

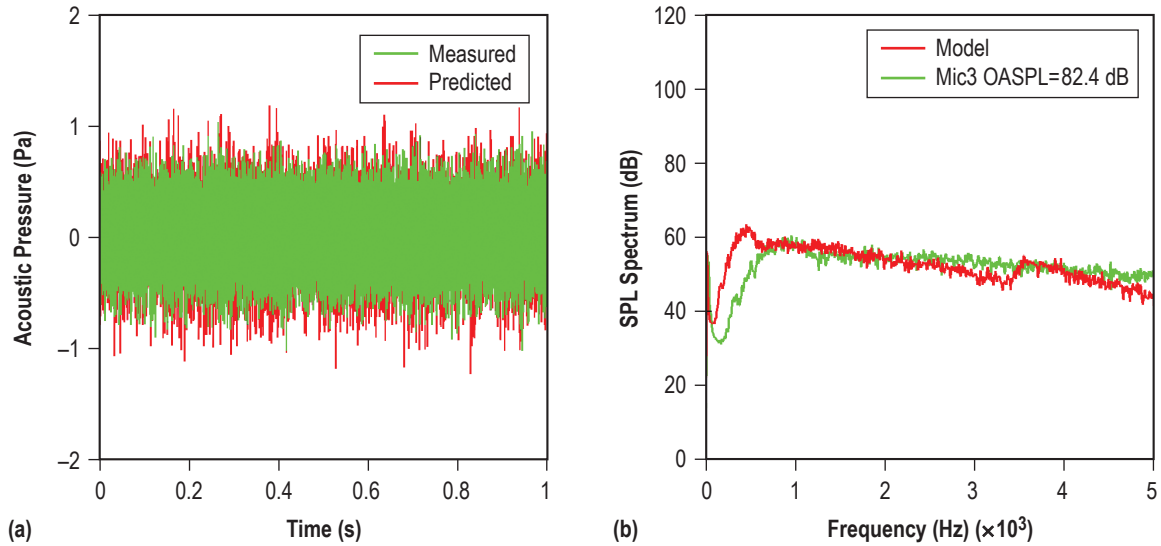


Figure 42. Mic3 location for a random frequency plane wave input: (a) Time history and (b) SPL spectrum.

Harmonic plane waves were also used for the long port at 500, 750, 1,000, 1,250, and 1,500 Hz. Figure 43 shows the various measured (green) and predicted (red) SPL spectrum. Good agreement is obtained between measured and predicted SPL spectra at all plane wave frequencies.

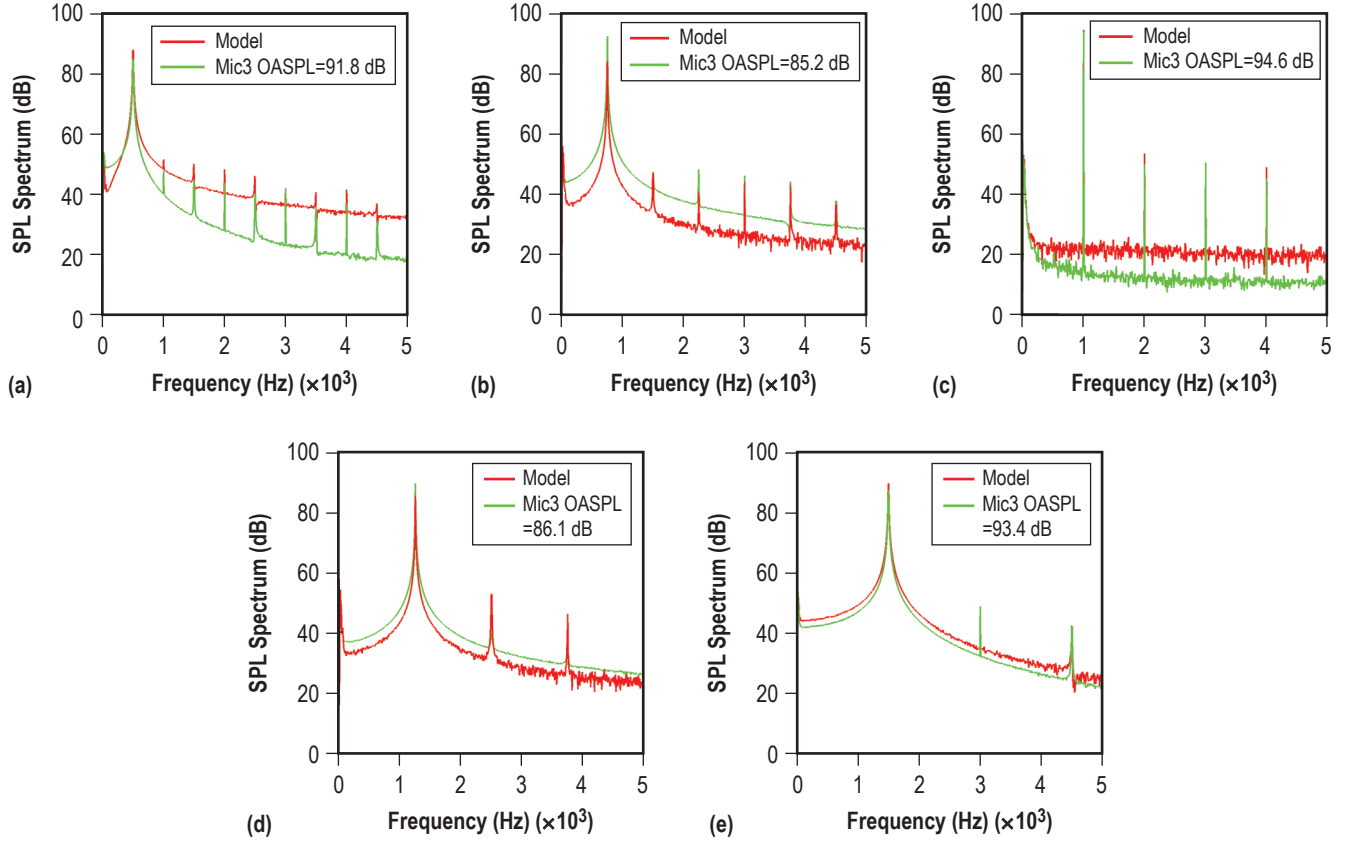


Figure 43. SPL spectrum at mic3 location for plane wave frequencies: (a) 500 Hz, (b) 750 Hz, (c) 1,000 Hz, (d) 1,250 Hz, and (e) 1,500 Hz.

5.2.2 Testing the Variable Temperature Model

In this section, the model developed in section 2.2 will be tested using both benchmark problems and experimental data. The data acquired did not have a temperature distribution, so applying the variable temperature model here is purely academic. First, the temperature-dependent wave equation is integrated using a fourth order Runge-Kutta method and the results compared to the exact analytical solution. Figure 44 shows the pressure distribution along the x -axis for a distance of 3 m and for an ambient temperature of 300 K (no temperature effect) obtained using both the Runge-Kutta scheme and the exact solution. The frequencies used are 500 and 1,000 Hz. Excellent agreement is obtained between the two solutions. Following the successful test of the Runge-Kutta scheme used to solve the wave equation, testing is now done on the WKB solution derived in section 2.2. Figure 45 shows a comparison of the solution obtained using the Runge-Kutta scheme and the WKB analytical solution. Good agreement is obtained at both frequencies. This comparison was obtained for $T(0) = 189$ K and $\alpha_T = 0.7 \text{ m}^{-1}$ using the profile described in section 2.2.

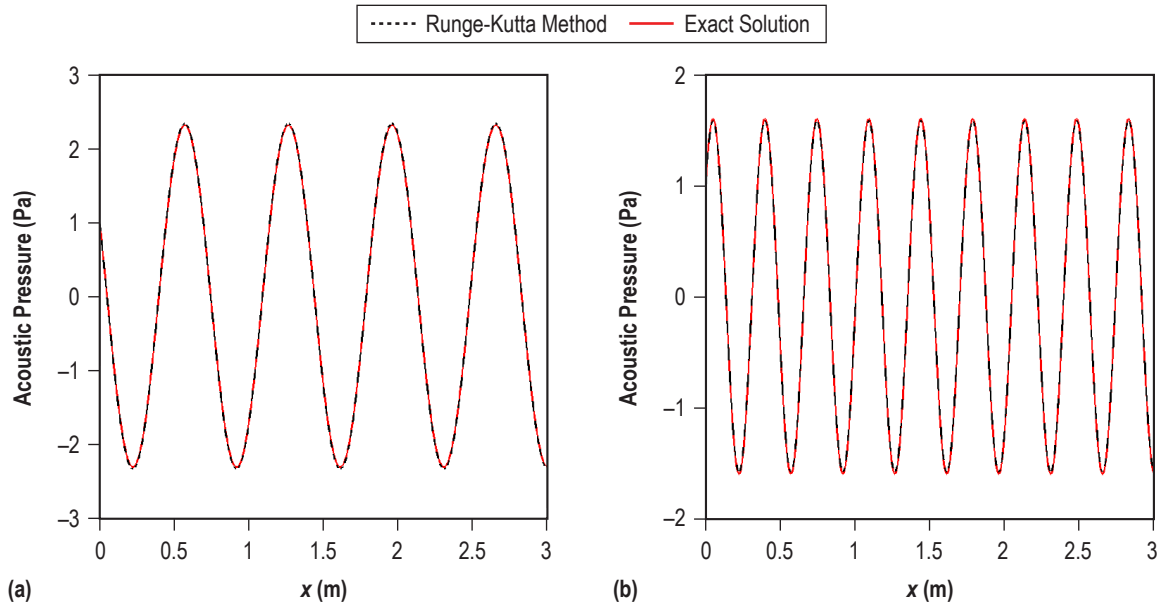


Figure 44. Pressure distribution along the x -axis obtained using the Runge-Kutta method and the exact solution for frequencies of (a) 500 Hz and (b) 1,000 Hz.

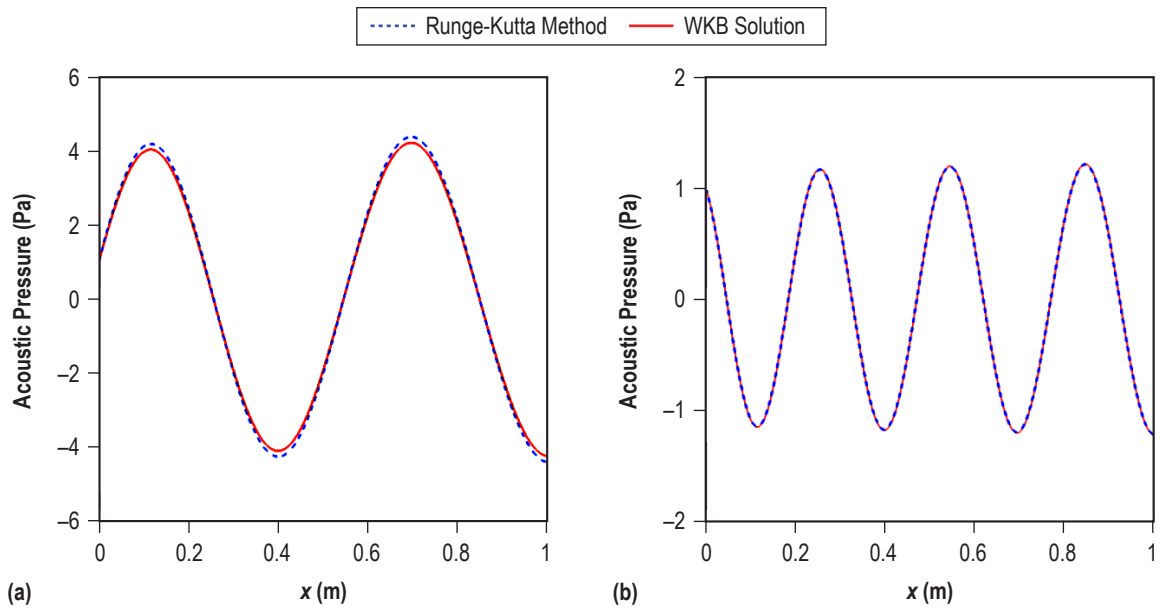


Figure 45. Pressure distribution along the x -axis obtained using the Runge-Kutta method and the WKB solution for frequencies of (a) 500 Hz and (b) 1,000 Hz.

6. CONCLUSIONS

It is clear from all the developments presented above that this project was very ambitious in scope as it covered all three areas of research—experimental, analytical, and computational. When the various tasks in the project were identified, the magnitude of the various hurdles to be resolved was not known and all tasks were thought to be doable within the 1 year time allotted. However, a year later, it is clear that some tasks are incomplete, especially the CFD tasks. However, the experimental work and the analytical modeling effort were very successful. CFD will be extended further into the near future. Following is a summary of all the achievements under this contract:

(1) Carried out several experiments and collected large amounts of data.

(2) Added a new experiment to the original list that consisted of measuring the pressure field inside a PVC pipe resulting from a harmonic plane wave. This was done to help the modeling effort while the primary experiment was being designed and readied for testing.

(3) Carried out the primary experiment consisting of a flat plate with sensor ports. The two sensor ports, one long and one short, had B&K microphones attached to them. The short port accommodated one microphone at the end of it, while the long port accommodated three microphones—one at the end and two along the port itself. Random, harmonic, and frequency sweep tests were carried out and time data at the various microphones were obtained and stored.

(4) Analyzed experimental data thoroughly and useful information such as transfer functions, power spectra, and SPL spectrum were obtained. Of particular importance was obtaining experimental values and graphs for the absorption coefficient plotted in figure 36.

(5) Developed analytical models for various experimental scenarios including a temperature gradient case. This was considered important as it addresses a problem encountered often in rocket engine testing where chamber temperatures can be in the 2,000 K range.

(6) Made comparisons of model predictions to experimental measurements. The developed models were used both in the forward direction and the reverse direction to predict either at the port back or port inlet. Overall, the models developed here were able to accurately predict the pressure field in the forward direction as well as in the reverse direction. The temperature gradient model could not be entirely tested as no experiment was run under those conditions.

(7) The CFD effort started late in the contract period as the experiments were delayed by equipment and software availability. Several issues were encountered in the CFD effort: gridding, boundary conditions, domain size, grid size, and computational resources available are some examples. All these issues were addressed in a timely manner, and primary results were obtained. These were not mature and not documented here.

(8) Certainly, the most important outcome of this contract from an academic institution viewpoint is the training of a Ph.D. student.

REFERENCES

1. Kinsler, L.E.; Frey, A.R.; Coppers, A.B.; and Sanders, J.V.: *Fundamentals of Acoustics*, 4th ed., Wiley & Sons, India, pp. 274–275, 1999.
2. Munjal, M.L.: *Acoustics of Ducts and Mufflers*, 2nd ed., Wiley, 416 pp., March, 17, 2014.
3. Selamet A.; Ji, Z.L.; and Kach, R.A.: “Wave reflections from duct terminations,” *J. Acoust. Soc. Am.*, Vol. 109, No. 4, pp. 1304–1311, April 2001.
4. Anno, P.D.: “A Klein–Gordon Acoustic Theory,” Doctor of Philosophy in Geophysics, Colorado School of Mines, Document No. T-4326, 1993.
5. Geiger, H.D.; and Daley, P. F.: “Finite Difference Modelling of the Full Acoustic Wave Equation in Matlab,” Acoustic Finite Difference Modeling, CREWES Research Report, Vol. 15, 2003.
6. Zhang, M.: “Reduced Order Models for the Turbulent Wall-Pressure Fluctuations and for Acoustic Wave Propagation in Sensor Ports,” Doctor of Philosophy in Mechanical and Aerospace Engineering, The University of Alabama—Huntsville, Huntsville, AL, 2015.
7. Kakar, R.: “Exact Solution of Non-Homogeneous Wave Equation by Conformal Mapping,” *Int. J. of Appl. Math and Mech.*, Vol. 9, No. 18, pp. 86–95, 2013.
8. Landau, L.D.; and Lifshitz, E.M.: *Course of Theoretical Physics: Mechanics*, Pergamon Press, Vol. 1, 1st Ed., 1960.
9. Leonhardt, U.: “Optical Conformal Mapping,” *Science*, Vol. 312. No. 5781, pp. 1777–1780, June 2006.
10. Rayleigh, J.W.S.; and Lindsay, R.B.: *The Theory of Sound, Volume 2*, (*Dover Classics of Science and Mathematics*), 2nd ed., Macmillan, London, pp. 319–326, 1896.
11. Tijdeman, H.: “On the propagation of sound waves in cylindrical tubes,” *J. Sound Vib.*, Vol. 39, No. 1, pp. 1–33, 1975.

REPORT DOCUMENTATION PAGE				Form Approved OMB No. 0704-0188	
<p>The public reporting burden for this collection of information is estimated to average 1 hour per response, including the time for reviewing instructions, searching existing data sources, gathering and maintaining the data needed, and completing and reviewing the collection of information. Send comments regarding this burden estimate or any other aspect of this collection of information, including suggestions for reducing this burden, to Department of Defense, Washington Headquarters Services, Directorate for Information Operation and Reports (0704-0188), 1215 Jefferson Davis Highway, Suite 1204, Arlington, VA 22202-4302. Respondents should be aware that notwithstanding any other provision of law, no person shall be subject to any penalty for failing to comply with a collection of information if it does not display a currently valid OMB control number.</p> <p>PLEASE DO NOT RETURN YOUR FORM TO THE ABOVE ADDRESS.</p>					
1. REPORT DATE (DD-MM-YYYY) 01-05-2016		2. REPORT TYPE Technical Publication		3. DATES COVERED (From - To)	
4. TITLE AND SUBTITLE Testing and Analysis of Sensor Ports				5a. CONTRACT NUMBER	
				5b. GRANT NUMBER	
				5c. PROGRAM ELEMENT NUMBER	
6. AUTHOR(S) M. Zhang,* A. Frendi,* W. Thompson,* and M.J. Casiano				5d. PROJECT NUMBER	
				5e. TASK NUMBER	
				5f. WORK UNIT NUMBER	
7. PERFORMING ORGANIZATION NAME(S) AND ADDRESS(ES) George C. Marshall Space Flight Center Huntsville, AL 35812				8. PERFORMING ORGANIZATION REPORT NUMBER M-1412	
9. SPONSORING/MONITORING AGENCY NAME(S) AND ADDRESS(ES) National Aeronautics and Space Administration Washington, DC 20546-0001				10. SPONSORING/MONITOR'S ACRONYM(S) NASA	
				11. SPONSORING/MONITORING REPORT NUMBER NASA/TP-2016-218222	
12. DISTRIBUTION/AVAILABILITY STATEMENT Unclassified-Unlimited Subject Category 71 Availability: NASA STI Information Desk (757-864-9658)					
13. SUPPLEMENTARY NOTES Prepared by the Propulsion Systems Department, Engineering Directorate *The University of Alabama—Huntsville					
14. ABSTRACT This Technical Publication summarizes the work focused on the testing and analysis of sensor ports. The tasks under this contract were divided into three areas: (1) Development of an Analytical Model, (2) Conducting a Set of Experiments, and (3) Obtaining Computational Solutions. Results from the experiment using both short and long sensor ports were obtained using harmonic, random, and frequency sweep plane acoustic waves. An amplification factor of the pressure signal between the port inlet and the back of the port is obtained and compared to models. Comparisons of model and experimental results showed very good agreement.					
15. SUBJECT TERMS sensor port, amplification factor, acoustic dissipation, absorption, attenuation, acoustics					
16. SECURITY CLASSIFICATION OF:			17. LIMITATION OF ABSTRACT UU	18. NUMBER OF PAGES 70	19a. NAME OF RESPONSIBLE PERSON STI Help Desk at email: help@sti.nasa.gov
a. REPORT U	b. ABSTRACT U	c. THIS PAGE U			19b. TELEPHONE NUMBER (Include area code) STI Help Desk at: 757-864-9658

National Aeronautics and
Space Administration
IS02

George C. Marshall Space Flight Center
Huntsville, Alabama 35812